

# Uncertainty quantification and estimation in differential dynamic microscopy

Mengyang Gu,<sup>1,\*</sup> Yimin Luo,<sup>2,3,\*</sup> Yue He,<sup>1</sup> Matthew E. Helgeson,<sup>2</sup> and Megan T. Valentine<sup>3,†</sup>

<sup>1</sup>*Department of Statistics and Applied Probability,  
University of California, Santa Barbara CA 93106, USA*

<sup>2</sup>*Department of Chemical Engineering, University of California, Santa Barbara CA 93106, USA*

<sup>3</sup>*Department of Mechanical Engineering, University of California, Santa Barbara CA 93106, USA*

(Dated: November 27, 2021)

Differential dynamic microscopy (DDM) is a form of video image analysis that combines the sensitivity of scattering and the direct visualization benefits of microscopy. DDM is broadly useful in determining dynamical properties including the intermediate scattering function for many spatiotemporally correlated systems. Despite its straightforward analysis, DDM has not been fully adopted as a routine characterization tool, largely due to computational cost and lack of algorithmic robustness. We present a comprehensive statistical framework that aims at quantifying error, reducing the computational order and enhancing the robustness of DDM analysis. We quantify the error, and propagate an independent noise term to derive a closed-form expression of the expected value and variance of the observed image structure function. Significantly, we propose an unbiased estimator of the mean of the noise in the observed image structure function, which can be determined experimentally and significantly improves the accuracy of applications of DDM. Furthermore, through use of Gaussian Process Regression (GPR), we find that predictive samples of the image structure function require only around 1% of the Fourier Transforms of the observed quantities. This vastly reduces computational cost, while preserving information of the quantities of interest, such as quantiles of the image scattering function, for subsequent analysis. The approach, which we call DDM with Uncertainty Quantification (DDM-UQ), is validated using both simulations and experiments with respect to accuracy and computational efficiency, as compared with conventional DDM and multiple particle tracking. Overall, we propose that DDM-UQ lays the foundation for important new applications of DDM, as well as to high-throughput characterization.

## I. INTRODUCTION

Microscopy has become an essential tool for probing dynamical processes in complex materials and systems, but typically requires sophisticated video image analysis to obtain quantitative information. Although real-space analysis methods retain information regarding individualistic processes within an image, feature tracking algorithms such as multiple particle tracking (MPT) are often computationally expensive and require user interactivity to determine algorithmic parameters to isolate the dynamical process(es) of interest [1, 2]. By contrast, Fourier transform-based analysis retains the statistical information encoded within the entire image, and is therefore more sensitive to low-signal processes as well as more robust to non-ideal imaging conditions and optically dense systems [3, 4]. In this way, Fourier microscopy combines the advantages of real-space imaging in feature identification and segmentation with ensemble-level statistical precision of Fourier-space analysis.

Of the various Fourier-space based approaches available, differential dynamic microscopy (DDM) [5] has emerged as a powerful and versatile analysis method to quantify spatiotemporally correlated dynamics from video microscopy data. This versatility stems from its

compatibility with a broad range of microscopy imaging modes, easy setup with instrumentation available in most research laboratories and straightforward analysis routines. DDM has been applied to study an ever-broadening range of phenomena in soft and biological matter systems [3, 4, 6], including analysis of the dynamics of concentrated particle suspensions [7], motions of swimming bacteria [8], and the coarsening dynamics of phase separating colloidal gels [9]. While it is common to assume the material to be isotropic, anisotropic properties such as the viscoelasticity of nematic liquid crystals can also be extracted [10].

For a more comprehensive overview of DDM and its various applications, the interested reader is referred to various reviews on the topic [3, 4, 11]. The present work is concerned with the development of a comprehensive statistical framework that aims at quantifying errors, reducing computational cost and enhancing the robustness of the analysis of differential dynamic microscopy (DDM) data. Similar developments have been made previously for MPT analysis [2, 12], and have greatly improved the robustness and algorithmic development of MPT in various applications. We therefore anticipate similar benefits from a more thorough investigation of uncertainty for DDM. To better motivate these developments, we first summarize the analysis procedure of DDM, and highlight the features and limitations of DDM that inspired the present study.

In DDM, a time sequence of image stacks represented by the intensity matrix  $I(\mathbf{x}, t)$  is processed using a Fourier-based technique where  $\mathbf{x} = (x_1, x_2)$  denotes two

\* Equal contribution

† Corresponding authors: mengyang@pstat.ucsb.edu; helgeson@ucsb.edu; valentine@engineering.ucsb.edu

spatial coordinates and  $t \in [t_{min}, t_{max}]$ . One first calculates the difference in intensity at each pixel location between two frames separated by a lag time  $\Delta t$ :

$$\Delta I(\mathbf{x}, t, \Delta t) = I(\mathbf{x}, t + \Delta t) - I(\mathbf{x}, t). \quad (1)$$

The intensity differences are then Fourier transformed and the absolute values squared to obtain the normalized squared intensity function in Fourier space:

$$|\Delta \hat{I}(\mathbf{q}, t, \Delta t)|^2 = |\mathcal{F}(\Delta I(\mathbf{x}, t, \Delta t))|^2, \quad (2)$$

where  $\mathcal{F}(\cdot)$  denotes the operator of the 2D discrete Fourier transformation (DFT),  $\mathbf{q} = (q_1, q_2)$  is a coordinate wave vector in reciprocal space.

The ensemble average of Eq. (2) is computed to obtain the dynamic image structure function  $D(\mathbf{q}, \Delta t)$ :

$$\begin{aligned} D(\mathbf{q}, \Delta t) &= \langle |\Delta \hat{I}(\mathbf{q}, t, \Delta t)|^2 \rangle \\ &= \frac{1}{n_{\Delta t} n_q} \sum_{t \in \mathcal{S}_{\Delta t}} \sum_{(q_1, q_2) \in \mathcal{S}_q} |\Delta \hat{I}(\mathbf{q}, t, \Delta t)|^2, \end{aligned} \quad (3)$$

where  $\langle \cdot \rangle$  denotes averaging across all instances of  $t \in \mathcal{S}_{\Delta t}$  and  $(q_1, q_2) \in \mathcal{S}_q$  with sets  $\mathcal{S}_{\Delta t} = \{t : t_{min} \leq t \leq t_{max} - \Delta t\}$ . The sizes of the two sets are denoted by  $n_{\Delta t} = \#\mathcal{S}_{\Delta t}$  and  $n_q = \#\mathcal{S}_q$ , respectively.

We only consider isotropic materials in this work, in which case  $D(\mathbf{q}, \Delta t) = D(q, \Delta t)$  where  $\mathcal{S}_q = \{(q_1, q_2) : q_1^2 + q_2^2 = q^2\}$ . However, the approach can be generalized to retain a multi-dimensional  $q$ -dependence as desired [13].

The following representation is routinely used to relate observables commonly associated with scattering analysis to the observations of  $D(q, \Delta t)$  [3, 5, 6]:

$$D_o(q, \Delta t) = A(q) (1 - f(q, \Delta t)) + B(q, \Delta t), \quad (4)$$

where  $A(q)$  is determined by the properties of the imaged material and imaging optics,  $B(q, \Delta t)$  is determined by the noise of the detection chain, and the subscript ‘o’ denotes the observed value. The intermediate scattering function (ISF),  $f(q, \Delta t)$ , is in principle the same as that measured in conventional light scattering measurements such as dynamic light scattering (DLS). The ISF quantifies how the dynamic structure decorrelates over the observed lengthscale  $1/q$  in Fourier space and timescale  $\Delta t$  in real space, which encodes the physical dynamics of the observed system. In general, for randomly-fluctuating, ergodic systems,  $f(q, \Delta t \rightarrow 0) = 1$  and  $f(q, \Delta t \rightarrow \infty) = 0$ , and thus,  $D_o(q, \Delta t \rightarrow 0) = B(q, \Delta t)$  and  $D_o(q, \Delta t \rightarrow \infty) = A(q) + B(q, \Delta t)$ .

DDM’s ultimate integration into the characterization workflows of a diverse range of systems is not without challenges. First, we note that, because DDM operates on a series of finite-exposure images taken of time-fluctuating processes, the measured DDM signal will contain inherent error related to both static and dynamic effects, much in the same way MPT incurs static and dynamic errors associated with the imaging process [12].

Because of this, the observed value  $D_o(q, \Delta t)$  will in general not be equal to the “true” image structure function  $D(q, \Delta t)$  that would be obtained from an ideal imaging system. Separating the signal from the noise in estimating the image structure function requires properly quantifying the uncertainty of the background noise that propagates through the analysis [5]. We will eventually show that  $D_o(q, \Delta t)$  typically overestimates  $D(q, \Delta t)$ , and that this inaccuracy stems primarily from imaging noise and associated uncertainty in the determination of  $B(q, \Delta t)$ . To our knowledge, there has yet to be a detailed analysis of the influence of imaging error on  $D_o(q, \Delta t)$ . Furthermore, there is currently no consensus view of an accurate estimator for  $B(q, \Delta t)$ . Several distinct methods have been proposed and used in prior studies. For example,  $B(q, \Delta t)$  has been assumed to be 0 [14], or estimated by the minimum value of  $D(q, \Delta t)$  at the temporal resolution  $\Delta t_{min}$ ,  $D_{min}(\Delta t_{min})$  [6]. Alternatively, in cases where the underlying physical processes are understood and a model of  $f(q, \Delta t)$  constructed,  $A(q)$  and  $B(q)$  can be treated as adjustable fitting parameters [8, 15, 16]. However, as we will ultimately show, none of these methods provides an unbiased estimator of the mean of  $B(q, \Delta t)$ . Rather, we show that such an estimator can be constructed through a formal analysis of error that propagates through the DDM analysis procedure from the acquired image sequence.

A second challenge of DDM analysis is the computational cost: the most computationally expensive step for DDM is performing a 2D fast Fourier transformation for each pixel of the difference for each image pairs ( $T \times (T-1)/2$  pairs, where  $T \sim 10^3 - 10^4$  is the total number of time points). For  $T$  images with size  $N \times N$  pixels ( $N \sim 10^2 - 10^3$ ), this requires  $O(T^2 N^2 \log_2(N))$  computational operations. Although there has been recent progress in accelerated computation that takes advantage of contemporary computational efficiency for Fourier-based image analysis [7, 17], these approaches still require resolving the DDM signal over the full sampled space of  $q$  and  $\Delta t$ .

The third, and often overlooked aspect, is the robustness of the algorithm(s) for decomposing  $D_o(q, \Delta t)$  into its more physically meaningful components through Eq. (4). To ensure applicability to a wide range of materials, it is desirable to allow for an arbitrary form of  $f(q, \Delta t)$ , such that the method does not require prior knowledge of the system’s dynamical properties. Moreover, the estimators used for  $A(q)$  and  $B(q)$  may contain bias, which can cause the algorithm to be less robust for both small and large lag times  $\Delta t$  in estimating  $f(q, \Delta t)$  and quantities derived from it [6].

An exemplifying context for the potential advantages gained by overcoming these limitations is the recent application of DDM to passive probe microrheology as an alternative to conventional approaches such as MPT [6, 18]. MPT-based passive probe microrheology involves imaging the Brownian fluctuations of embedded colloidal probes in order to resolve their mean square displace-

ments (MSD)  $\langle \Delta r^2(\Delta t) \rangle$  [1], which in the limit of homogeneous, uniform materials can be related to their linear viscoelastic moduli [19, 20]. DDM offers an alternative approach to MPT in estimating the MSD through the estimation of  $f(q, \Delta t)$  using Eq. (4). DDM presents a number of advantages in this regard, including applicability and better statistical precision to low-signal or optically dense probes and materials [6, 21–23]. Importantly, since DDM requires no *a priori* user-input parameters associated with the probes or imaging system, it has the potential to provide automated, user-free and non-biased analysis that could enable high-throughput characterization [11]. However, as alluded to previously, realizing this capability requires accurate and non-biased determination of  $f(q, \Delta t)$ , and therefore provides further motivation for the current study.

In this work, we make three contributions towards overcoming these challenges in DDM: (1) we quantify the error in image intensity and propagate it throughout the analysis; (2) we speed up the computation by using Gaussian Process Regression (GPR) [24] to overcome the computational bottleneck introduced by the Fourier transformations by subsampling the data at selected  $\Delta t$  and  $q$  (Figure 1); and (3) we use predictive samples from GPR to robustly estimate the image structure function, mean squared displacement and other quantities of interest. Furthermore, we derive an unbiased estimator of the mean of the background noise in the image structure function, which improves the accuracy of MSD and other quantities of interests at small  $\Delta t$ .

## II. METHODOLOGY

We name our new algorithm *Differential Dynamic Microscopy with Uncertainty Quantification* (DDM-UQ). The analysis routine is described schematically in Figure 1. First, image stacks  $I(\mathbf{x}, t)$  are acquired with a microscope or are produced using a particle dynamics simulation algorithm. The background noise term  $\sigma_0^2$  of intensity is also assessed. Then, a small subsample of roughly 1% of the image differences are squared and Fourier transformed to construct a set of observed quantities  $D_o(\mathbf{q}, \Delta t)$ . Thereafter, GPR is fit to  $D_o(\mathbf{q}, \Delta t)$  to obtain a predictive distribution  $D(q, \Delta t)$ . Eventually, the predictive samples for each  $q$  are used to obtain predictive samples for quantities of interest (such as  $f(q, \Delta t)$  and  $\langle \Delta r^2(\Delta t) \rangle$ ). Through analysis of a number of simulated and experimental datasets, we demonstrate that our new approach not only reduces the computational time, but in many cases also improves the accuracy and robustness of estimation, as compared to previous DDM approaches and MPT.

### A. Error quantification

To develop a statistical approach to error quantification and analysis, we write the observed intensity as

$$I_o(\mathbf{x}, t) = I(\mathbf{x}, t) + \epsilon(\mathbf{x}, t), \quad (5)$$

where  $I(\mathbf{x}, t)$  is an (unknown) deterministic function of the observed sample and imaging system;  $\epsilon(\mathbf{x}, t)$  is an independent random noise with mean zero and variance  $\sigma_0^2$ ; the subscript ‘o’ denotes the observed value. Several artifacts are known to impact the accuracy of DDM and are expected to contribute to  $\epsilon(\mathbf{x}, t)$ , including camera detection noise, edge effects arising from the finite field of view [25] and effects of finite exposure time [14]. Others are known to affect MPT, such as the depth of tracking [2] and finite pixel size [12], and are expected to impact DDM as well. Here we consider  $\epsilon(\mathbf{x}, t)$  to be the difference between the measured signal and the “true” intensity  $I(\mathbf{x}, t)$  at each pixel without regard to the actual physical origin of the error. We note that there are other known spatially or temporally correlated artifacts, such as illumination fluctuations, that do not satisfy the criteria assumed for  $\epsilon(\mathbf{x}, t)$ . These will not be considered in the present analysis.

We illustrate how the error in Eq. (5) propagates in the analysis of DDM. The derivation of Eq. (6)- Eq. (10) is given in Appendix A. Assuming that Eq. (5) holds, we can express the observed squared intensity function in reciprocal space as

$$\begin{aligned} |\Delta \hat{I}_o(\mathbf{q}, t, \Delta t)|^2 &= |\Delta \hat{I}(\mathbf{q}, t, \Delta t)|^2 + 2\Delta \hat{I}(\mathbf{q}, t, \Delta t)\Delta \hat{\epsilon}(\mathbf{q}, t, \Delta t) \\ &\quad + |\Delta \hat{\epsilon}(\mathbf{q}, t, \Delta t)|^2, \end{aligned} \quad (6)$$

where the closed form expressions of  $|\Delta \hat{I}(\mathbf{q}, t, \Delta t)|^2$ ,  $\Delta \hat{I}(\mathbf{q}, t, \Delta t)\Delta \hat{\epsilon}(\mathbf{q}, t, \Delta t)$  and  $|\Delta \hat{\epsilon}(\mathbf{q}, t, \Delta t)|^2$  are given in Eq. (30)-(32) in Appendix A, respectively.

The expected value (i.e. mean) of  $|I_o(\mathbf{q}, t, \Delta t)|^2$  is given by

$$\mathbb{E}[|\hat{I}_o(\mathbf{q}, t, \Delta t)|^2] = |\Delta \hat{I}(\mathbf{q}, t, \Delta t)|^2 + 2\sigma_0^2. \quad (7)$$

Note that the mean of the cross-product term,  $\langle \Delta \hat{I}(\mathbf{q}, t, \Delta t)\Delta \hat{\epsilon}(\mathbf{q}, t, \Delta t) \rangle$ , is zero under the assumptions made for  $\epsilon(\mathbf{x}, t)$ .

By combining Eq. (3) and Eq. (6), we can express the observations of the dynamic image structure function as follows:

$$\begin{aligned} D_o(q, \Delta t) &= \langle |\Delta \hat{I}(\mathbf{q}, t, \Delta t)|^2 \rangle + 2\langle \Delta \hat{I}(\mathbf{q}, t, \Delta t)\Delta \hat{\epsilon}(\mathbf{q}, t, \Delta t) \rangle \\ &\quad + \langle |\Delta \hat{\epsilon}(\mathbf{q}, t, \Delta t)|^2 \rangle, \end{aligned} \quad (8)$$

where  $\langle \cdot \rangle$  denotes the ensemble with respect to  $\mathbf{q} \in \mathcal{S}_q$  and  $t \in \mathcal{S}_{\Delta t}$ . The mean of  $D_o(q, \Delta t)$  follows

$$\mathbb{E}[D_o(q, \Delta t)] = D(q, \Delta t) + 2\sigma_0^2. \quad (9)$$

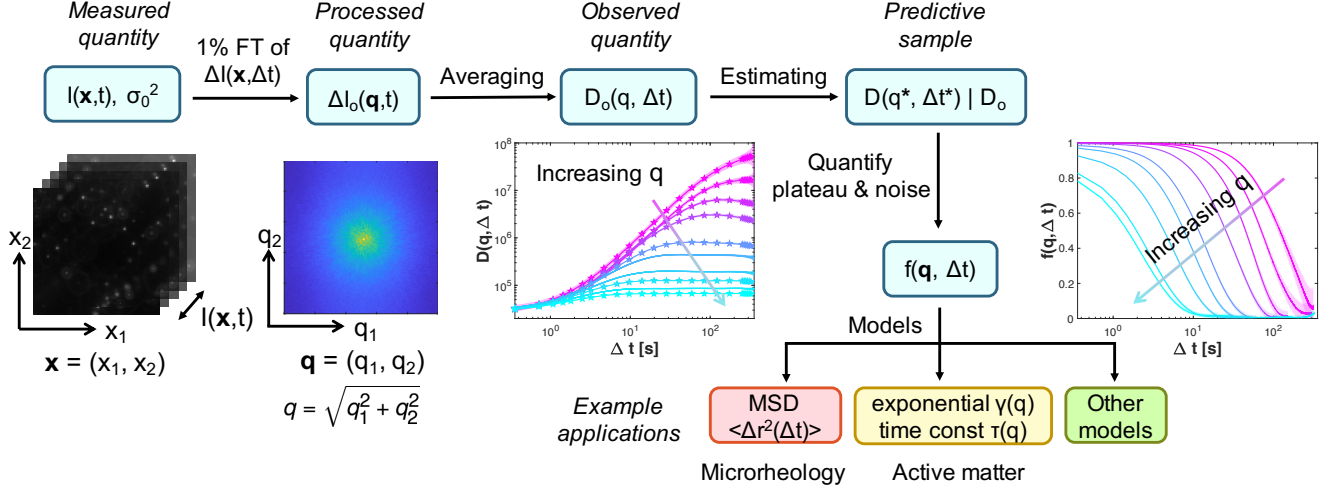


FIG. 1. Schematic representation of DDM-UQ-based data reduction, sampling and fitting procedure used to determine material constants. From the stack of images acquired by microscopy, around 1% of the Fourier transforms are performed to obtain the observed image structure function  $D_o(q, \Delta t)$ , from which a predictive sample is generated to estimate  $D(q^*, \Delta t^*)$  at unobserved  $q^*$  and  $\Delta t^*$ , given  $D_o(q, \Delta t)$ . In the graphs of  $D_o(q, \Delta t)$  versus  $\Delta t$  and  $f(q, \Delta t)$  versus  $\Delta t$ , at select  $q$ 's, the stars denote data selected for fitting, the lines denote values at all  $\Delta t$ 's for a particular  $q$ . The shadow denotes 95% predictive interval, which is small compared to the range of the change in  $D(q, \Delta t)$  over the range of  $\Delta t$ . The predictive samples preserve the quantiles of the distribution after transformation and are then used to find material quantities of interest.

Further assuming  $\epsilon(\mathbf{x}, t) \sim \mathcal{N}(0, \sigma_0^2)$  independently, we can calculate the variance

$$\mathbb{V}[D_o(q, \Delta t)] = \frac{2\sigma_0^2}{n_q n_{\Delta t}} \left( 2\sigma_0^2 + 2D(q, \Delta t) + \max(0, (T - 2\Delta t)) \left( \frac{\sigma_0^2}{n_{\Delta t}} - \frac{2S_{q, \Delta t}}{(T - 2\Delta t)n_{\Delta t}n_q} \right) \right), \quad (10)$$

where the expression of  $S_{q, \Delta t}$  is given in Eq. (34) in Appendix A.

The result in Eq. (10) is intuitive: the ratio  $\frac{1}{n_q n_{\Delta t}}$  arises from the fact that the  $D_o(q, \Delta t)$  is averaged from  $n_q$  and  $n_{\Delta t}$  observations of  $\langle \hat{I}(\mathbf{q}, t, \Delta t)^2 \rangle$ , as shown in Eq. (3), which decreases the variance. The other terms arise from the covariance between the *sin* and *cos* terms from the Fourier transform and that of the recursive sampling of the same image in different  $\Delta t$ , but these terms play lesser roles.

Note that by Eq. (9), an unbiased estimator of  $D(q, \Delta t)$  is  $D_o(q, \Delta t) - 2\sigma_0^2$ , while using the observations  $D_o(q, \Delta t)$  alone typically overestimates the image structure function by  $2\sigma_0^2$  on average. Potential practical procedures for independently estimating  $2\sigma_0^2$  will be discussed later.

We have shown that  $D_o(q, \Delta t)$  can be separated into a deterministic term of the signal ( $D(q, \Delta t)$ ) and a random term containing the noise and cross product of the noise and signal. This representation can be related to Eq. (4) by letting

$$B(q, \Delta t) = 2\langle \Delta \hat{I}(\mathbf{q}, t, \Delta t) \Delta \hat{\epsilon}(\mathbf{q}, t, \Delta t) \rangle + \langle |\Delta \hat{\epsilon}(\mathbf{q}, t, \Delta t)|^2 \rangle, \quad (11)$$

where the mean

$$\mathbb{E}[B(q, \Delta t)] = 2\sigma_0^2, \quad (12)$$

and the variance

$$\mathbb{V}[B(q, \Delta t)] = \mathbb{V}[D_o(q, \Delta t)], \quad (13)$$

in Eq. (10). We observe that specifying  $B$  as 0 typically underestimates the noise, while specifying  $B$  as the minimum value  $D(q, \Delta t_{min})$  overestimates the mean of the noise by an amount given by Eq. (9). Furthermore, if  $A(q)$  can be correctly estimated or calculated, then an unbiased estimator for  $B$  naturally improves estimates of  $f(q, \Delta t)$ . In the case where  $A(q)$  is unknown, the improvement in estimating  $f(q, \Delta t)$  diminishes at large  $\Delta t$ , where the estimation of the plateau  $D(q, \Delta t \rightarrow \infty)$  more strongly impacts the value of  $f(q, \Delta t)$  at these  $\Delta t$  values.

For applications of DDM to microrheology, and assuming dilute probes with diffusive particle dynamics involving Gaussian displacements, we can relate the MSD  $\langle \Delta r^2(\Delta t) \rangle$  at each  $q$  to the image structure function and related quantities as follows [6, 26]:

$$f(q, \Delta t) = \exp\left(-\frac{q^2 \langle \Delta r^2(\Delta t) \rangle}{4}\right) \left[ 1 + \frac{\alpha_2 q^4 \langle \Delta r^2(\Delta t) \rangle^2}{32} + \dots \right], \quad (14)$$

where the first order non-Gaussian parameter  $\alpha_2 = \frac{d \langle r^4(\Delta t) \rangle}{(d+2) \langle \Delta r^2(\Delta t) \rangle^2} - 1$  ( $d$ =dimensionality) is a measure of the heterogeneity or non-diffusive dynamics of the sample [27]. As is common in microrheology, we assume the

contribution of the non-Gaussian parameter is negligible [19], and thus  $\Delta r^2(q, \Delta t)$  at each  $q$  can be inverted from  $D(q, \Delta t)$  through the following approach:

$$\begin{aligned} \Delta r^2(q, \Delta t) &= \frac{4}{q^2} \ln \left[ \frac{A(q)}{A(q) - D(q, \Delta t) + B(q, \Delta t)} \right] \\ &= \frac{4}{q^2} \ln \left[ \frac{D(q, \Delta t_{q, \max}) - B(q, \Delta t)}{D(q, \Delta t_{q, \max}) - D(q, \Delta t)} \right], \end{aligned} \quad (15)$$

where  $D(q, \Delta t_{q, \max})$  denotes the apparent plateau value of the dynamic image structure function at each  $q$  (i.e.  $f(q, \Delta t_{q, \max}) = 0$ ). It is common to assume sample ergodicity, and use the ensemble average of  $\Delta r^2(q, \Delta t)$  to estimate the mean squared displacement  $\langle \Delta r^2(\Delta t) \rangle$ . We also note that  $D_o(q, \Delta t)$  is often used to estimate  $D(q, \Delta t)$  at any  $q$  and  $\Delta t$ .

To illustrate the importance of proper error estimation, we consider the outcomes of three different ways of estimating  $B$  (Figure 2) on  $\langle \Delta r^2(\Delta t) \rangle$ , which was previously reported to be highly sensitive to the estimated value of  $B$ , particularly for small  $\Delta t$  [6]. If there exists  $\Delta t_{q, \min}$ , such that  $D_o(q, \Delta t_{q, \min}) = D_{\min}(\Delta t_{\min})$  for a given  $q$ , and  $B$  is estimated by  $D_{\min}(\Delta t_{\min})$  (red solid line), then from Eq. (15), the argument of the natural log approaches unity, and  $\Delta r^2(q, \Delta t_{q, \min}) \rightarrow 0$ , which in turn drives  $\log_{10}(\Delta r^2(q, \Delta t_{q, \min})) \rightarrow -\infty$ , as shown.

On the other hand, if  $B$  is estimated to be 0 (green solid line), then approximately  $\log_{10}(\Delta r^2(q, \Delta t \rightarrow 0)) \rightarrow \log_{10} \left[ \frac{4}{q^2} \ln \left( \frac{D_o(q, \Delta t_{q, \max})}{D_o(q, \Delta t_{q, \max}) - 2\sigma_0^2} \right) \right]$  (an asymptotic value denoted by the green dotted line), as the expected value of  $D_o(q, 0)$ ,  $\mathbb{E}(D_o(q, 0)) = 2\sigma_0^2$ . When we use the correct estimator  $B = 2\sigma_0^2$  (blue solid line), the estimated  $\Delta r^2(q, \Delta t) \rightarrow 0$  when  $\Delta t \rightarrow 0$ .

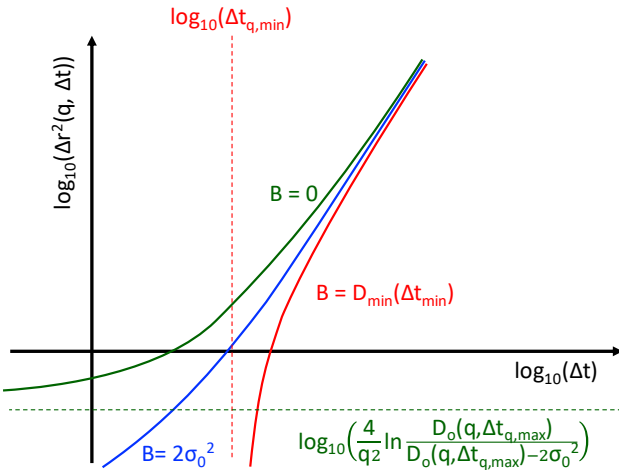


FIG. 2. Illustration of how three different approaches to estimating  $B$  influence the calculated MSD. For given  $q$ , the quantity  $\Delta t_{q, \min}$  satisfies  $D_o(q, \Delta t_{q, \min}) = D_{\min}(\Delta t_{\min})$  and  $\Delta t_{q, \max}$  is the time difference where  $D_o(q, \Delta t_{q, \max})$  first reaches the ‘plateau’.

These asymptotic limits demonstrate the crucial importance of properly estimating the mean of  $B$  by  $\sigma_0^2$

when extracting dynamical properties from DDM such as the ISF or MSD, particularly at small  $\Delta t$ , a result that is further validated in various simulated and experimental examples (see e.g. Fig. 3 (d) and Fig. 4). A similar point about  $B$  was noted previously by other researchers: while uncertainty in  $A(q)$  is considered to dominate the analysis because it pertains to the signal, overestimating  $B(q)$  such as in [6] can lead to spurious results when computing  $\langle \Delta r^2(\Delta t) \rangle$  [18], and hence the authors proposed an iterative scheme to solve for  $\langle \Delta r^2(\Delta t) \rangle$ . In experiment, the noise term,  $\sigma_0^2$ , can be measured, typically through independent experiments using immobilized particles under identical imaging conditions. The variance of the image difference is then computed to give  $\sigma_0^2$ . In MPT, a “noise floor” is commonly quantified [12] and frequently subtracted from all data to give a more realistic estimate of the MSD [28–30]; however, such characterization is not currently routine for DDM.

## B. Gaussian Process Regression

The other challenges in DDM are the computational bottleneck that arises when performing a massive number of Fourier transformations, as well as limitations to the robustness of the algorithm when the noise is relatively large. We overcome these problems by a Gaussian process regression model, a widely used machine learning tool for estimating nonlinear latent surfaces [24]. We use as little as 1% of the data to estimate the image structure function and to filter spurious noise. In the following derivation, the natural logarithm of the wave vector (in reciprocal space) and time are denoted by  $(\tilde{q}, \tilde{t}) = (\ln(q), \ln(\Delta t)) = \boldsymbol{\theta}$  and the natural logarithm of the image structure function is denoted by  $\tilde{D}_o(\boldsymbol{\theta}) = \ln(D_o(\boldsymbol{\theta}))$ . We model the intensity by

$$\tilde{D}_o(\boldsymbol{\theta}) = \tilde{D}(\boldsymbol{\theta}) + \epsilon_{\boldsymbol{\theta}}, \quad (16)$$

where  $\epsilon_{\boldsymbol{\theta}}$  is a zero mean Gaussian noise with variance  $\sigma_{\boldsymbol{\theta}}^2$ . The latent function  $\tilde{D}(\cdot)$  is modeled by a Gaussian process, meaning that any marginal distribution  $\tilde{\mathbf{D}} = (\tilde{D}(\boldsymbol{\theta}_1), \dots, \tilde{D}(\boldsymbol{\theta}_n))^T$  at  $n$  inputs  $\{\boldsymbol{\theta}_1, \dots, \boldsymbol{\theta}_n\}$  follows a multivariate normal distribution:

$$(\tilde{D}(\boldsymbol{\theta}_1), \dots, \tilde{D}(\boldsymbol{\theta}_n))^T \mid \mathbf{m}, \mathbf{R}, \sigma^2 \sim \mathcal{MN}(\mathbf{m}, \sigma^2 \mathbf{R})$$

where  $\mathbf{m} = (m(\boldsymbol{\theta}_1), \dots, m(\boldsymbol{\theta}_n))^T$  is a vector of the mean (assumed to be a constant in this work, i.e.  $\mathbf{m} = (m, \dots, m)^T$ ) and  $\sigma^2 \mathbf{R}$  is an  $n \times n$  covariance matrix where the  $(i, j)$ -th term is parameterized by a covariance function  $\sigma^2 K(\cdot, \cdot)$ .

The power (stretched) exponential covariance function and Matérn covariance function are often used for GPR [24]. For any two inputs  $\boldsymbol{\theta}_a = (\tilde{q}_a, \tilde{t}_a)$  and  $\boldsymbol{\theta}_b = (\tilde{q}_b, \tilde{t}_b)$ , we use a product covariance function  $\sigma^2 K(\boldsymbol{\theta}_a, \boldsymbol{\theta}_b) = \sigma^2 K_1(\tilde{q}_a, \tilde{q}_b) K_2(\tilde{t}_a, \tilde{t}_b)$ , with  $K_l(\cdot, \cdot)$ ,  $l = 1, 2$  following a Matérn correlation with roughness

parameter  $5/2$  such that

$$K_l(x_a, x_b) = \left(1 + \sqrt{5}\beta_l d + \frac{5\beta_l^2 d^2}{3}\right) \exp\left(-\sqrt{5}\beta_l d\right), \quad (17)$$

where  $d = |x_a - x_b|$  for any real valued input  $x_a$  and  $x_b$  with inverse range parameter  $\beta_l \in \mathbb{R}^+$ ,  $l = 1, 2$ . The sample path of the Gaussian process with Matérn correlation in (17) is twice differentiable and is often used as a default correlation in GPR [31].

Let  $\tilde{\mathbf{D}}_o = (\tilde{D}_o(\boldsymbol{\theta}_1), \dots, \tilde{D}_o(\boldsymbol{\theta}_n))^T$  denote the  $n$  observations. The parameters in the Gaussian process contain mean parameter  $m$ , variance parameter  $\sigma^2$  and inverse range parameters  $\boldsymbol{\beta} = (\beta_1, \beta_2)$  in the kernel function. Conditional on  $\boldsymbol{\beta}$  and the nugget parameter  $\eta$ , the maximum likelihood estimator of the mean parameter is  $\hat{m} = (\mathbf{1}_n^T \tilde{\mathbf{R}}^{-1} \mathbf{1}_n)^{-1} \mathbf{1}_n^T \tilde{\mathbf{R}}^{-1} \tilde{\mathbf{D}}_o$ , with  $\tilde{\mathbf{R}} = \mathbf{R} + \eta \mathbf{\Lambda}$  and  $\mathbf{\Lambda}$  is an  $n \times n$  diagonal matrix with the  $i$ th diagonal term being  $\hat{\sigma}_i^2 / (\eta \sigma^2)$  (a fixed parameter discussed later) and  $\hat{\sigma}^2 = S^2 / n$  with  $S^2 = (\tilde{\mathbf{D}}_o - \mathbf{1}_n \hat{m})^T \tilde{\mathbf{R}}^{-1} (\tilde{\mathbf{D}}_o - \mathbf{1}_n \hat{m})$ . Plugging the  $(\hat{m}, \hat{\sigma}^2)$ , the profile likelihood of parameters  $(\boldsymbol{\beta}, \eta)$  in the covariance function follows  $\mathcal{L}(\boldsymbol{\beta}, \eta) \propto |\mathbf{K}|^{-\frac{1}{2}} (S^2)^{-\frac{n}{2}}$ . Since no closed formed expression of the maximum likelihood estimator for the range and nugget parameters is available, one often numerically maximizes the profile likelihood to obtain the estimates of  $(\boldsymbol{\beta}, \eta)$ . When the sample size is small, the MLE can be unstable and marginal posterior mode estimation with robust parameterization is often used [32]. We implemented the parameter estimation and predictions of GPR in the ‘RobustGaSP’ package available in R and MATLAB [31].

Conditional on the estimated parameters  $(\hat{m}, \hat{\sigma}^2, \hat{\boldsymbol{\beta}}, \hat{\eta})$ , the predictive distribution of  $\tilde{D}_o(\boldsymbol{\theta}_*)$  at any  $\boldsymbol{\theta}_*$  follows a normal distribution [24]

$$(\tilde{D}_o(\boldsymbol{\theta}_*) | \tilde{\mathbf{D}}_o, \hat{m}, \hat{\sigma}^2, \hat{\boldsymbol{\beta}}, \hat{\eta}) \sim \mathcal{N}(\tilde{D}_*(\boldsymbol{\theta}_*), \hat{\sigma}^2 K_*(\boldsymbol{\theta}_*, \boldsymbol{\theta}_*) + \tilde{\sigma}_*^2), \quad (18)$$

where  $\tilde{\sigma}_*^2$  is the variance of the noise  $\epsilon_{\boldsymbol{\theta}_*}$  with

$$\tilde{D}_*(\boldsymbol{\theta}_*) = \hat{m} + \mathbf{r}_{\boldsymbol{\theta}_*}^T \tilde{\mathbf{R}}^{-1} (\tilde{\mathbf{D}}_o - \hat{m} \mathbf{1}_n) \quad (19)$$

$$K_*(\boldsymbol{\theta}_*, \boldsymbol{\theta}_*) = \hat{\sigma}^2 \left( K(\boldsymbol{\theta}_*, \boldsymbol{\theta}_*) - \mathbf{r}_{\boldsymbol{\theta}_*}^T \tilde{\mathbf{R}}^{-1} \mathbf{r}_{\boldsymbol{\theta}_*} \right), \quad (20)$$

where  $\mathbf{r}_{\boldsymbol{\theta}_*} = (K(\boldsymbol{\theta}_1, \boldsymbol{\theta}_*), \dots, K(\boldsymbol{\theta}_n, \boldsymbol{\theta}_*))^T$ . The predictive median  $\tilde{D}_*(\boldsymbol{\theta}_*)$  is often used for predicting  $\boldsymbol{\theta}_*$ . The predictive median of  $D_o(\boldsymbol{\theta}_*)$  can be obtained by transforming the predictive median of  $\tilde{D}_o(\boldsymbol{\theta}_*)$  through the natural exponential function.

The predictive median in (19) can be written as a weighted average of observations:

$$\tilde{D}_*(\boldsymbol{\theta}_*) = \mathbf{w} \tilde{\mathbf{D}}_o, \quad (21)$$

where  $\mathbf{w} = (1 - \mathbf{r}_{\boldsymbol{\theta}_*}^T \tilde{\mathbf{R}}^{-1} \mathbf{1}_n) (\mathbf{1}_n^T \tilde{\mathbf{R}}^{-1} \mathbf{1}_n)^{-1} \mathbf{1}_n^T \tilde{\mathbf{R}}^{-1} + \mathbf{1}_n^T \tilde{\mathbf{R}}^{-1}$  is an  $1 \times n$  row vector of weights. For a zero mean GP (i.e.  $m = 0$ ), the weights simply become  $\mathbf{w} = \mathbf{r}_{\boldsymbol{\theta}_*}^T \tilde{\mathbf{R}}^{-1}$ . The weights in the predictive median are

determined by penalizing misfit by squared errors and the complexity of fit by the native norm [24], as the predictive median in (19) is equivalent to the kernel ridge regression (KRR) estimator below

$$\hat{h}_n = \underset{h \in \mathcal{H}}{\operatorname{argmin}} \left\{ \frac{1}{n} (\tilde{D}_o(\tilde{\boldsymbol{\theta}}_i) - h(\tilde{\boldsymbol{\theta}}_i))^2 + \lambda \|h\|_{\mathcal{H}}^2 \right\}, \quad (22)$$

where  $\mathcal{H}$  is a reproducing kernel Hilbert space (RKHS) and  $\|\cdot\|_{\mathcal{H}}$  denotes the RKHS norm (or native norm) [24]. The KRR is widely used as a surrogate model for emulating computationally expensive simulations or latent functions (see e.g. [33–40]). See e.g. ([41]) for a brief review of the connection between GPR and KRR, as well as their applications in physics. One advantage of GPR is that the uncertainty of prediction is given in the predictive distribution in Eq. (18), whereas KRR only provides a point estimator. The predictive distribution of GPR will be used to generate samples to approximate other quantities of interests such as intermediate scattering functions and MSDs.

### C. Predictive sampling by a downsampled data set

After obtaining the image intensities, DDM-UQ analysis starts by selecting approximately 1% of the design points equally spaced logarithmically along the input space coordinates to compute  $D_o(q, \Delta t)$  as shown in Figure 3a. The Fourier transformation is only performed on this reduced set of image differences, allowing for fast, high-throughput analysis. Since an estimate of the plateau of the image structure function at long times is often required by the analysis, we ensure that at least 5 design points lie on the interval  $[0.7\Delta t_{max}, 0.9\Delta t_{max}]$  on the  $\Delta t$ -axis for each chosen  $\tilde{q}$  (Fig. 3b).

A homogeneous noise is often assumed in GPR, i.e.  $\tilde{\sigma}_{\boldsymbol{\theta}}^2 = \tilde{\sigma}^2$ . Here since the number of pixels used in obtaining  $D_o(q, \Delta t)$  is  $n_q n_{\Delta t}$ , the variance of the noise may be specified as  $\tilde{\sigma}_{\boldsymbol{\theta}}^2 \propto 1/(n_q n_{\Delta t})$ .

The predictive median of  $D_o(q, \Delta t)$  is smoother than the observed  $D_o(q, t)$  since spurious noise is effectively filtered out (see e.g. the black curves and blue curves in Fig 3b). Consequently, identifying the long-time ‘plateau’ of  $D_o(q, \Delta t)$  by the predictive median from GPR for each  $q$  is more robust than using  $D_o(q, \Delta t)$  directly. Here we simply let the ‘plateau’ of  $D_o(q, \Delta t)$  be the maximum value of the predictive median at  $\Delta t \in [0.7\Delta t_{max}, 0.9\Delta t_{max}]$  for each  $q$ , which greatly simplifies the approach in estimating downstream quantities such as the ISF and MSD. This assumption applies to most thermally driven systems, but it can be problematic for cases where the video is too short to realize complete decay of  $f(q, \Delta t)$ , for which there is expected to be non-ergodic behavior such that  $f(q, \Delta t) \neq 0$  at  $\Delta t \rightarrow \infty$ , or in atypical cases where the fundamental objects contributing to the intensity exhibit time fluctuation in their intensity profiles that do not decorrelate over time, such



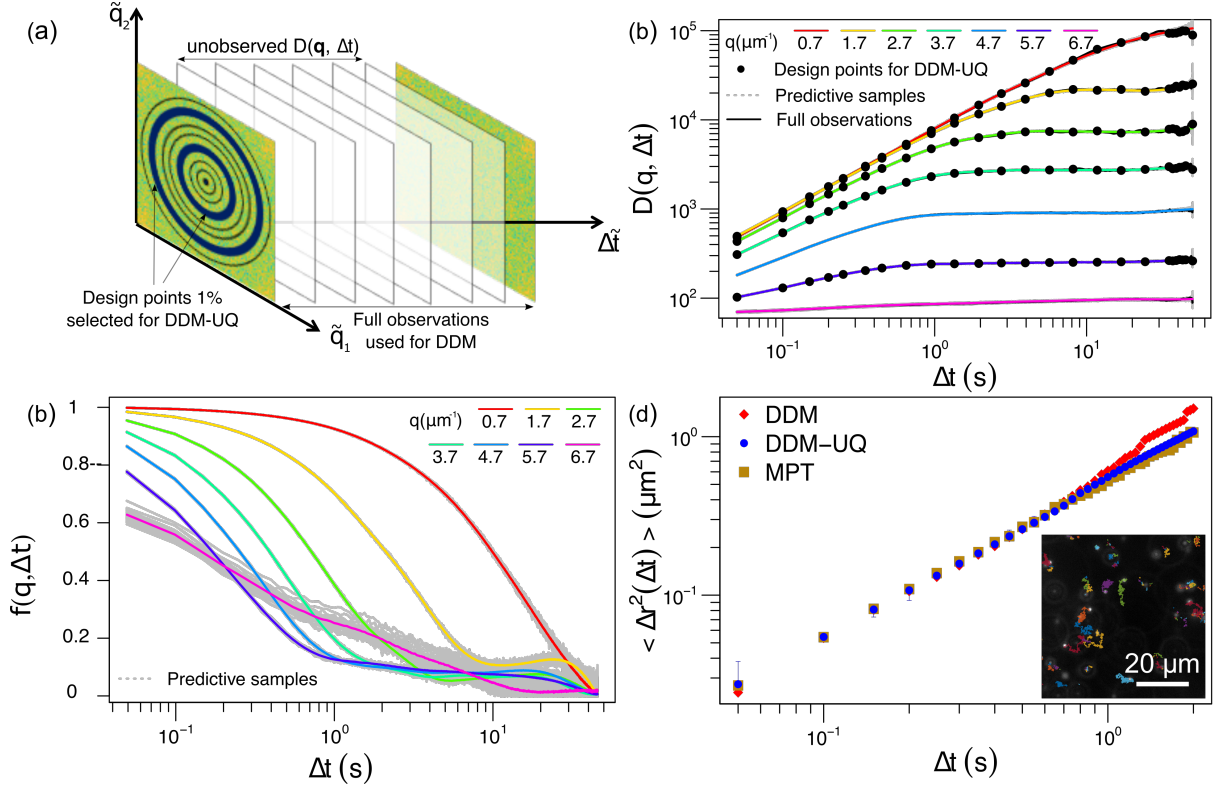


FIG. 3. (a) The design points (blue circles) are selected along the logarithmically scaled coordinates  $(\mathbf{q}, \Delta t)$ , requiring only a fraction of the Fourier transformations to compute  $D_o(\mathbf{q}, \Delta t)$ . (b) Predictive median and predictive samples by GPR for representative values of  $q$ 's. The variance of noise is proportional to the inverse of the number of pixels in ensemble. Only 30 predictive samples are shown (grey dashed line), while 300 samples for each  $q$  are generated to obtain statistical quantities. The observations used for GPR are plotted as black dots. The full observations (black lines) overlap with the predictions (colored lines). (c) The predictive samples for the intermediate scattering function is plotted against the lag time. (d) Predictive mean squared displacement is plotted against the lag time using all three methods. The 95% predictive interval is shown with the error bar for DDM-UQ. The inset shows a snapshot of experiment with MPT trajectory overlay. Plots (b-d) are derived from a movie of with  $1 \mu\text{m}$  probe particles diffusing in a viscous fluid.

that  $A(q, \Delta t)$  retains a time dependence that is not constant at long time. In Section III E, we illustrate such a case; in that case, the plateau is more appropriately determined by the mean value of the predictive median at  $\Delta t \in [0.7\Delta t_{max}, 0.9\Delta t_{max}]$  for each  $q$ .

Note that our goal is not only to predict the median or mean of  $D_o(q, \Delta t)$  for the unsampled input  $(q, \Delta t)$  values, but rather to relate  $D_o(q, \Delta t)$  to other quantities of interest, such as the intermediate scattering function  $f(q, \Delta t)$  or mean squared displacement  $\langle \Delta r^2(\Delta t) \rangle$ , both of which are nonlinear transformations of  $D_o(q, \Delta t)$ . To achieve this, we sample image structure functions from the predictive distribution in Eq. (18) and transform the samples to obtain other quantities of interest. The transformed predictive samples can be used to estimate the predictive interval of quantities of interest at a given set of input  $(q, \Delta t)$ . In this work, we sample 300 observations, denoted as  $D_s(q, \Delta t)$  for  $s = 1, 2, \dots, 300$  at any  $(q, \Delta t)$ , and transform  $D_s(q, \Delta t)$  to obtain other quantities of interest, such as intermediate scattering function  $f_s(q, \Delta t)$  via Eq. (4) after estimating the ‘plateau’

value,  $D_s(q, \Delta t \rightarrow \infty) = A(q) + B(q)$ , and the noise term at each  $q$ . For each  $(q, \Delta t)$ , the 95% predictive interval of  $f(q, \Delta t)$  can be estimated by the lower 2.5% quantile and the upper 2.5% quantile of the transformed predictive samples  $f_s(q, \Delta t)$  for  $s = 1, 2, \dots, 300$ .

After specifying the ‘plateau’ value of the image structure function at each  $q$  using this approach, the predictive samples are used to estimate  $f(q, \Delta t)$  and  $\langle \Delta r^2(\Delta t) \rangle$  shown in Fig. 3c-d. Conditional on the observed values  $D_o(q, \Delta t)$ , the predictive samples obtained from the GPR ensure proper error propagation in each step. Furthermore, here the predictive samples preserve information such as quantiles of distribution for any transformation.

### III. VALIDATION THROUGH SIMULATION

#### A. Image formation and analysis approach

To validate our methodology, we first employ simulations of a time series of images demonstrating particle

motion. This approach has the significant advantage that the true particle motion is known *a priori* and the true MSD has a closed form expression, thus allowing quantitative comparison with results obtained using DDM, DDM-UQ, and MPT, the latter obtained using an open source tracking algorithm [42]. Moreover, it is possible to investigate systematically how different sources of noise influence algorithm performance, and whether different functional forms of  $\langle \Delta r^2(\Delta t) \rangle$  perform differently.

We first examine simulated video images of particles in motion, each with a Gaussian intensity profile with peak intensity  $I_c = 255$  and standard deviation of  $\sigma_p = 2$  pixels. In principle, the intensity recorded at a single pixel  $I_p(\mathbf{x})$  could arise from intensity contributions of multiple particles in the vicinity. The contribution of the  $j$ -th particle located in  $\mathbf{x}_j(t)$  is given by:

$$I_p(\mathbf{x}, \mathbf{x}_j(t)) = I_c \exp\left(-\frac{(\mathbf{x} - \mathbf{x}_j(t))^2}{2\sigma_p^2}\right). \quad (23)$$

To account for noise in the background intensity signal, a time-varying, random uniform noise  $I_b(\mathbf{x}, t)$ , centered around zero, in the range  $[-10, 10]$  is added. Thus, we may compute  $\sigma_0^2$  as the variance of the background noise  $I_b(\mathbf{x}, t)$ :  $\sigma_0^2 = \frac{(10 - (-10))^2}{12} \approx 33.3$ . Thus, the signal at a time  $t$  is the sum of signals attributed to all particles as well as the background:

$$I(\mathbf{x}, t) = I_b(\mathbf{x}, t) + \sum_{j=1}^{n_p} I_p(\mathbf{x} - \mathbf{x}_j(t)). \quad (24)$$

Note that the pixel intensities in simulation are not subjected to a cut-off ceiling value as are those obtained in imaging (e.g. 0-255 for an 8-bit image). Moreover, unlike MPT, where the relative brightness of particle and background significantly affects tracking precision [12], in DDM signal quality depends sensitively on the magnitude of the image difference. Keeping this context in mind, we simulate particles with brightness  $I_p(\mathbf{x} - \mathbf{x}_j(t))$  that does not vary with time, and we vary the step size by which the particles move in each time step instead. It is well-known that DDM performance deteriorates, and can completely break down, in the limit of small probe displacement [6]. For diffusive particles taking a step with a variance  $\sigma_s^2$ , we compare the performance of DDM, DDM-UQ, and MPT in calculating the MSD values.

For the conventional DDM analysis, we perform the Fourier transformation of all values of  $\Delta I(\mathbf{x}, \Delta t)$ , and estimate  $B(q)$  using the minimum of  $D(q, \Delta t)$  over all  $q$  at  $\Delta t_{min}$ . Following the procedure of [6], we use the following plateau estimation and data selection process. For each  $q$ , the last 10% of  $D(q, \Delta t)$  are truncated since not enough image pairs are averaged, leading to poor statistics. The  $D(q, \Delta t)$  in the range of 70-90%  $\Delta t$  are considered to be “plateau” values and their mean and variance are computed over 70-90%  $\Delta t$ . Any value of  $q$  where the variance exceeds a preset value of 0.02 in normalized pixel intensity is rejected and does not contribute to calculating the  $\langle \Delta r^2(\Delta t) \rangle$ . Additionally, any  $q$  values for

which  $D(q, \Delta t)$  exceeds 80% of the “plateau” value are also excluded due to the divergence of the denominator as shown in Eq. (15). For accepted values of  $q$ ,  $A(q) + B(q)$  is given by the mean “plateau” value.

The DDM-UQ analysis represents data obtained using our proposed approach based on the downsampled Fourier transformation of  $\Delta I(\mathbf{x}, \Delta t)$ ’s with GPR and predictive samples. Unless specified, The mean of the noise is estimated by the measured  $2\sigma_0^2$  in DDM-UQ. MPT was performed by locating particles in each frame, and searching in the vicinity to link trajectories of individual particles. The localization error is not characterized, given the high particle intensity compare to the background intensity in all cases investigated.

In all cases, we generated videos of the motion of  $n_p = 50$  particles, except for the case in Section IIIB, where  $n_p = 800$ . The simulation box is a 2D square with sides  $L = 480$ . The movie spans time steps  $t = 1, 2, \dots, 1000$ . We further imposed displacements in each successive time step  $\Delta x_{i,j}(t) = x_{i,j}(t+1) - x_{i,j}(t)$  (where  $i = 1, 2$  stands for the  $x_1$ , or  $x_2$  directions in the Cartesian coordinates in 2D).

We construct three scenarios that represent the general features observed in a broad range of experiments: simple diffusion, diffusion with drift, and constrained diffusion within a harmonic potential well (i.e. an Ornstein-Uhlenbeck process). These scenarios will result in distinct shapes of  $\langle \Delta r^2(\Delta t) \rangle$  and highlight various challenges to each analytical approach. The derivations of the expected values of the MSDs for all simulated scenarios are given in Appendix B.

As a metric of the accuracy of a given analysis method, we compare the normalized root mean squared error (N-RMSE) for the estimated MSD relative to the known true MSD:

$$\text{N-RMSE} = \frac{\sqrt{\frac{1}{n_{\Delta t}} \sum_{\Delta t \in \Delta \mathcal{T}} (\langle \Delta \tilde{r}^2(\Delta t) \rangle - \langle \Delta \tilde{r}_e^2(\Delta t) \rangle)^2}}{\tilde{\sigma}_r}, \quad (25)$$

where  $\langle \Delta \tilde{r}^2(\Delta t) \rangle$  is the logarithm of the true MSD with base 10,  $\langle \Delta \tilde{r}_e^2(\Delta t) \rangle$  is the corresponding estimate using DDM, DDM-UQ or MPT, and  $\tilde{\sigma}_r$  is the sample standard deviation of the logarithm of the true MSD with base 10. In practice, not all  $\Delta t$  values are available for every method, due to large fluctuations at large  $\Delta t$  values, and this provides a limit to the total lag time range captured in each case. To ensure that the three methods are evaluated on the same test set  $\Delta \mathcal{T}$  and ease quantitative comparisons, we determine the usable range of  $\Delta t$ ’s by the smallest maximum lag time available among the three methods. The N-RMSE of different simulated cases is summarized in Table I.



TABLE I. N-RMSE of simulated cases. MPT does not converge for the first scenario, as the number of particles is  $n_p = 800$ , which is very dense optically.

Scenario	DDM	DDM-UQ	MPT
Simple diffusion, $\sigma_s = 2$ , optically dense	0.231	0.035	N.D.
Simple diffusion, $\sigma_s = 2$	0.133	0.025	0.022
Simple diffusion, $\sigma_s = 0.5$	0.187	0.054	0.067
Simple diffusion, $\sigma_s = 4$	0.252	0.023	0.492
Diffusion with drift	0.974	0.057	0.017
Diffusion with drift, optically dense	0.073	0.016	0.596
O-U process with drift	0.373	0.154	0.043

N.D. = not determined

### B. Validating the use of $\sigma_0^2$ as an estimator for $B$

We have shown that  $2\sigma_0^2$  is an unbiased estimator of the mean of  $B$ , and that the estimation of  $\sigma_0^2$  is critically important to the analysis of DDM data. To illustrate this point, we first show results of a simulation of  $n_p = 800$  particles moving in a purely viscous fluid. We generate movies demonstrating simple Brownian motion: at each time step,  $\Delta x_{i,j}(t) \sim \mathcal{N}(0, \sigma_s^2)$  independently, where  $\sigma_s$  represents step size with units of pixels. The expected MSD of the Brownian motion is  $\mathbb{E}(\langle \Delta r^2(\Delta t) \rangle) = 2\sigma_s^2 \Delta t$ . For 2D diffusive motion, we thus expect  $\langle r^2(\Delta t) \rangle = 4D_m \Delta t$ , where  $D_m$  is the diffusion coefficient.  $D_m$  can be associated with the step size  $D_m = \frac{\sigma_s^2}{2}$ . For  $\sigma_s^2 = 4$ ,  $D_m = 2$  and the truth is  $\langle r^2(\Delta t) \rangle = 4D_m \Delta t = 8\Delta t$ .

Figure 4 shows the MSDs calculated by each of the following: the conventional DDM algorithm with an estimate of  $B = D_{min}(\Delta t_{min})$  (red diamonds); our proposed DDM-UQ algorithm using  $B = 2\sigma_0^2$  (blue circles), and DDM-UQ using  $B = 0$  (green triangles). The truth is plotted as the thick black line. As we expect, using DDM-UQ with the unbiased estimator of the mean of  $B$ ,  $\sigma_0^2$ , outperforms the other methods in accurately identifying the true MSD. Choosing  $B = 0$  tends to overestimate the true MSD, while choosing  $B = D_{min}(\Delta t_{min})$  tends to underestimate the true MSD. These results are consistent with the effects illustrated in Fig. 2. The algorithmic limitations are most pronounced at small  $\Delta t$  because the displacements are smaller and therefore more strongly impacted by a poorly estimated noise term. As a result, the N-RMSE for estimating MSD by the DDM-UQ approach based on around 1% of observations with  $B$  estimated to be  $\sigma_0^2$  is smaller than that by DDM with  $B$  estimated to be  $D_{min}(t_{min})$ , shown in the first row of Table I. Thus, in the sections to follow,  $2\sigma_0^2$  is used to estimate  $B$  in the DDM-UQ analysis of all simulated and experimental scenarios.

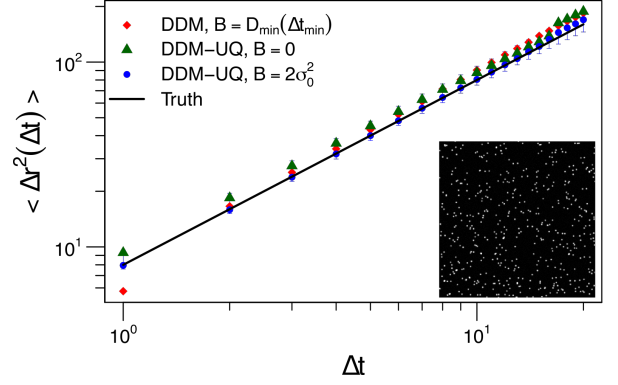


FIG. 4. The ensemble-averaged MSD calculated from the simulated 2D Brownian motion of 800 particles. The red diamonds represent the MSD estimated using conventional DDM, based on analysis of all data of  $D(q, \Delta t)$  with  $B = D_{min}(\Delta t_{min})$ . The green triangles and blue circles represent the estimated MSDs based on 1% of  $D(q, \Delta t)$  using weighed Gaussian process regression for predictions with  $B = 0$  and  $B = \sigma_0^2$ , respectively. The error bars denote 95% predictive interval when the mean of  $B = 2\sigma_0^2$ . The truth of  $\langle \Delta r^2(\Delta t) \rangle = 8\Delta t$  is denoted as the black line. The inset shows the initial position of particles, where particles are enlarged for better visualization. Note that it is not possible to perform MPT due to the large number of particles moving within the frame.

### C. Simple diffusion with different step size $\sigma_s$

To explore the effects of varying step size (diffusivity) on our analysis, three additional scenarios with diffusive dynamics are explored, using simulations of particles taking different step sizes  $\sigma_s$ , but for which all other settings and conditions were held constant. When  $\sigma_s = 2$ , corresponding to an intermediate step size, all three methods (DDM, DDM-UQ and MPT) provide results that reasonably approximate the true values that are directly calculated from the inputted particle positions (Fig. 5a). When the N-RMSE values are calculated and compared, we find that the results from MPT provide the best approximation of the true values, while DDM-UQ provides nearly the same level of accuracy as MPT (Table I). By contrast, DDM performs relatively poorly.

We next calculated the MSDs for simple diffusion with lower ( $\sigma_s = 0.5$ ) and higher ( $\sigma_s = 4$ ) step sizes (Fig. 5b-c). As the step size decreases (Fig. 5b,  $\sigma_s = 0.5$ ), the N-RMSEs increase for all three analysis routines, with the most significant performance deterioration observed with DDM (Table I). However, the largest differences are observed at high step size, (Fig. 5c) where particle displacements are large ( $\sigma_s = 4$ ). In this limit, DDM-UQ vastly outperforms both DDM and MPT (Table I). The reason is intuitive for MPT: as particle displacement becomes large, the likelihood of two or more particles exchanging positions within the search radius increases significantly. This can lead to the algorithm misidentifying the particle, thereby resulting in erroneous linking of the trajec-

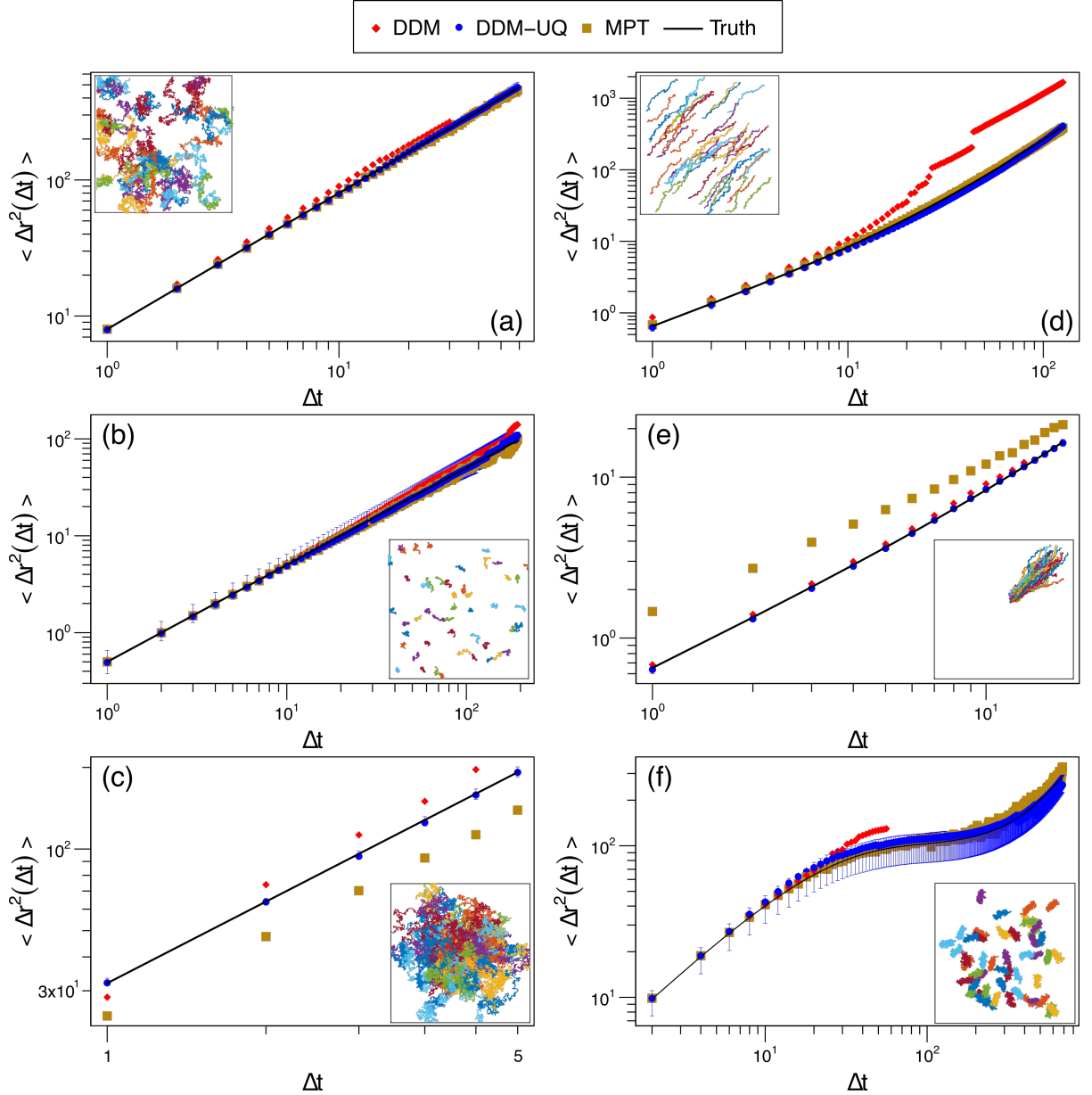


FIG. 5. Comparisons of MSDs calculated using DDM-UQ, DDM and MPT for various simulated scenarios: (a-c) simple diffusion with (a)  $\sigma_s = 2$  (b)  $\sigma_s = 0.5$  and (c)  $\sigma_s = 4$ , corresponding to intermediate, low and high step sizes. (d-e) diffusion with drift in (d) optically dilute and (e) optically dense samples, and (f) diffusion of a particle within a harmonic potential well (Ornstein-Uhlenbeck process) subjected to drift. The blue error bars depict the mean and 95% predictive interval estimated by DDM-UQ based on 1% of the  $D(q, \Delta t)$ , respectively. The red markers indicate mean values estimated using the conventional DDM algorithm based on all values of  $D(q, \Delta t)$ . The golden squares and black solid line represent the output of MPT analysis and the true values as directly calculated from the known particle positions, respectively. The generated particle trajectories are shown in the insets, in a simulation box of 480 pixels by 480 pixels.

tories. On the other hand, the conventional approach to DDM, which uses the  $D_{min}(\Delta t_{min})$  as the estimator for  $B$ , misrepresents the noise in this regime. In general, this effect is more pronounced when the signal is large, since the bias by  $D_{min}(\Delta t_{min})$  is also large.

#### D. Diffusion with drift

We next consider particles subjected to diffusive-convective motion (i.e. “drift”). At each time step, a particle moves by  $\Delta x_{i,j} \sim \mathcal{N}(\mu_D, \sigma_s^2)$ , resulting in a random walk with step size  $\sigma_s = 0.56$  superimposed on a deterministic drift with mean velocity  $\mu_D = 0.1$  in units of pixels/time step in the same direction for all parti-

cles. The expected value of the MSD in this case is  $\mathbb{E}[\langle \Delta r^2(\Delta t) \rangle] = 2\sigma_s^2 \Delta t + 2\mu_D^2 \Delta t^2$ . At short  $\Delta t$ , the motion is primarily diffusive (Fig. 5d),  $\langle \Delta r^2(\Delta t) \rangle \sim \Delta t$  with a transition to convective motion,  $\langle \Delta r^2(\Delta t) \rangle \sim \Delta t^2$ , at large  $\Delta t$ . This results in an increasing value of  $\frac{d\langle \Delta r^2(\Delta t) \rangle}{d\Delta t}$  with  $\Delta t$ , and permits a measure of the relative strength of the two dynamic processes through measure of the local slope on a log-log scale.

We also compare the performance of the different analytical routines under differing initial conditions. In particular, we vary the initial positions where particles were released at  $t = 1$ , holding all other settings equal, to compare an optically dilute scenario (Fig. 5d), where particles were uniformly distributed throughout the simulation box, and an optically dense scenario (Fig. 5e), where particles were released from a small  $\frac{L}{20} \times \frac{L}{20}$  square in the middle of the frame causing them to be near each other and even overlap for some frames. When particles are evenly distributed in the simulation box, conventional DDM still overestimates the MSD at large  $\Delta t$ , which is attributed to the large fluctuations in  $D(q, \Delta t)$ . The simulation mimics situations where a high concentration of particles are present, which are also known to lead to tracking issues in MPT since it often fails to distinguish particles in close proximity. By contrast, DDM and DDM-UQ perform strongly in this limit (Table I), with lower errors for DDM-UQ. The range of  $\Delta t$  that can be resolved by any method decreases as compared to the dilute case. However, DDM-UQ provides a larger range of  $\Delta t$ , as compared to DDM, due to its ability to smooth over  $D(q, \Delta t)$  providing usable data in the long  $\Delta t$  regime that were discarded in conventional DDM due to excessive fluctuations in the plateau regime.

### E. Ornstein-Uhlenbeck process with drift

Finally, we simulated particles from an Ornstein-Uhlenbeck (O-U) process with drift. Such a process mimics thermally-driven particle motion in an effective elastic medium with drifts distinct to each particle. The convective term is constant in magnitude  $\mu_D$ , and fixed in direction  $\theta$  for an individual particle, but randomized for all particles. A pure O-U process without a convective term can lead to a  $\langle \Delta r^2(\Delta t) \rangle$  that plateaus at a certain  $\Delta t$ , and thus  $f(q, \Delta t)$  does not decorrelate for some finite values of  $\Delta t$ . Adding a convective term leads to complete decorrelation and allows the dynamics at these  $\Delta t$ 's to be captured. Moving the sample to achieve ensemble averaging for sample that manifested constrained heterogeneity has previously been applied to light scattering on polymer gel samples [43].

Here, just like the original O-U process, successive steps have a weak correlation with previous steps:

$$X_{i,j}(t+1) = \rho X_{i,j}(t) + \epsilon_{i,j,t}, \quad (26)$$

where  $\epsilon_{i,j,t} \sim \mathcal{N}(0, \sigma_s^2(1 - \rho^2))$ , with  $\rho = 0.95$ ,  $\sigma_s = 5$  and  $X_{i,j}(t) = x_{i,j}(t) - (t-1)\mu_{ij} - x_{i,j}(1)$  for any  $t$ ; the

indices represent the  $j$ -th particle and  $i$ -th direction ( $i = 1, 2$ ) and  $\mu_{1j} = \mu_D \cdot \cos\theta_j$ ,  $\mu_{2j} = \mu_D \cdot \sin\theta_j$ , respectively, with  $\mu_D = 0.02$ . The particles' initial position was generated by a normal distribution centered around  $x_{ij}(t_0)$  with variance  $\sigma_s^2$ , i.e.  $x_{ij}(t_1) \sim \mathcal{N}(x_{ij}(t_0), \sigma_s^2)$ , where  $x_{ij}(t_0)$  are randomly distributed within a square  $\frac{3L}{4} \times \frac{3L}{4}$  in the middle of the simulation box to reduce the likelihood that a particle moves out of the frame during the simulation. The motion is subject to an attractive potential towards  $x_{ij}(t_0) + (t-1)\mu_{ij}$  with drift  $(\mu_D \cos(\theta_j), \mu_D \sin(\theta_j))^T$  at the  $t$ th time point for the  $j$ th particle. The expected value of MSD for O-U process with drift is  $\mathbb{E}[\langle \Delta r^2(\Delta t) \rangle] = 4\sigma_s^2(1 - \rho^{\Delta t}) + \mu_D^2 \Delta t^2$ . There is a diffusive contribution that dominates at sufficiently small  $\Delta t$  from the first term,  $1 - \rho^{\Delta t} \approx 1 - (1 + \ln(\rho)\Delta t) = \ln(\rho^{-1})\Delta t$ , by Taylor expansion at small  $\Delta t$ . The second convective term captures the convective flow, and can represent the type of dynamics observed in some actively driven systems [44, 45].

The process results in a trace of MSD versus lag time with multiple inflection points:  $\langle \Delta r^2(\Delta t) \rangle$  first grows with decreasing slope until the plateau value is reached ( $\frac{d\langle \Delta r^2(\Delta t) \rangle}{d\Delta t} \approx 0$ ); at much longer lag times, the MSD will grow with an increasing slope until eventually the convective motion dominates ( $\frac{d\langle \Delta r^2(\Delta t) \rangle}{d\Delta t} = 2$ ). In contrast to all previous scenarios, we find that  $D(q, \Delta t)$  exhibits non-monotonic behavior and that the MSD shows apparent  $q$ -dependence over  $\Delta t$  for many intermediate  $q$  values. Specifically, a local maximum in  $D(q, \Delta t)$  appears before  $D(q, \Delta t)$  reaches the plateau at long  $\Delta t$ . Such non-monotonic behavior in the resulting  $f(q, \Delta t)$  has previously been observed by in a system consisting of self-catalytic Janus particles [14]. By definition of  $A(q) = D(q, \Delta t \rightarrow \infty) - B(q)$ , the mean values of  $D(q, \Delta t)$  in the range of  $[0.7\Delta t_{max}, 0.9\Delta t_{max}]$  is thus the more appropriate choice for estimating  $A(q)$  for each  $q$  in this particular case *en route* to computing the MSD.

We find that both MPT and DDM-UQ are able to capture the general trends and magnitude of motion (Fig. 5f). At short  $\Delta t$ , the response of all three methods is similar. We note that this scenario constitutes an “ideal” case for MPT: the particle locations are sparse, and each particle moves toward their respective attractive centers,  $x_{ij}(t_0)$ , never to cross paths with one another. Consistent with this, MPT is able to capture dynamics at long  $\Delta t$  (Fig. 5f). DDM-UQ more accurately follows the truth than DDM at small  $\Delta t$  owing to the proper accounting of the weights at small  $\Delta t$ 's, using weighted GPR (see Section IIB). The estimation at large  $\Delta t$  is inherently difficult for both DDM and DDM-UQ due to limited numbers of observations and instability at large  $\Delta t$ . DDM cannot accurately capture the MSD even before the sub-diffusive plateau. Still, with limited sampling, DDM-UQ vastly outperforms DDM at large  $\Delta t$  and its performance approaches that of MPT. How to more accurately estimate the MSD at large  $\Delta t$  is an open research question for DDM-UQ, and is important for tracking the dynamics of slowly-evolving systems. The N-RMSE reflects these

observations (Table I).

Overall, we find that DDM-UQ accurately determines  $\langle \Delta r^2(\Delta t) \rangle$  for a range of experimentally-relevant scenarios based on a very limited amount of information (around 1% of the observations). Many other scenarios abound where  $f(q, \Delta t)$  rather than the MSD can provide physical insight to the system. Nevertheless, we find that the MSD provides a particularly sensitive test of the performance of the DDM-UQ compared to conventional DDM because of its ability to stabilize large fluctuations inherent to limited data sampling. These findings affirm the sensitivity of this ensemble-based method as well as the need for an unbiased estimator, and validates our data reduction approach.

#### IV. ANALYSIS OF EXPERIMENTAL DATA

##### A. Determination of imaging noise $\sigma_0^2$

While DDM has the advantage of ample statistics, the accuracy of the measurement hinges upon the accurate assessment of the noise term. Therefore, a robust method for determining  $\sigma_0^2$  is critical. In the case of MPT, this determination is often performed by taking an image series of a control sample under identical optical conditions and frame rates, with identical particles and concentrations, and using identical sample geometries as in the actual experiments, but with the particles immobilized in a solid matrix. To isolate the particle motions due to artifactual fluctuations in this work, we immobilize particles in a stiff crosslinked polyethylene-glycol (PEG) hydrogel consisting of 10 wt% 4-arm PEG-Norbornene (molecular weight = 5k, Creative PEGWorks, Research Triangle Park, NC) and 3 wt% hexa(ethylene glycol) dithiol, with photoinitiator 2-hydroxy-2-methylpropiophenone added at 1 wt% of the 4-arm PEG-Norbornene, which is crosslinked under ultraviolet illumination for 5 minutes at room temperature. The material stiffness ensures that the thermally-driven particle motions are not resolvable on experimental timescales, thus the apparent measured particle displacements report only the motions due to equipment vibrations, light fluctuations, etc. To our knowledge, this is the first work that explicitly quantifies imaging noise for DDM analysis.

##### B. Newtonian fluid

We first measured the properties of a Newtonian fluid in which we expect simple diffusive particle dynamics. Experimentally, we suspended fluorescent polystyrene microspheres of diameter  $2a = 100$  nm (yellow-green with excitation maxima of  $\lambda_{ex} = 441$  nm and emission maxima at  $\lambda_{em} = 485$  nm, Polysciences, Warrington, PA) in a 30 wt% sucrose solution (Sigma-Aldrich, St. Louis, MO) at a particle volume fraction  $\phi \approx 3 \times 10^{-5}$ . This composition

was previously studied by dark-field DDM [46], and that study provides a reference data set to which we can compare our results. The particle suspension is introduced into a home-made sample cell formed using a glass slide and glass cover slip separated by 100  $\mu\text{m}$  spacers. The sample is imaged in epifluorescence using an Olympus IX73 inverted microscope, outfitted with a halogen lamp with green fluorescent protein (GFP) filter set ( $\lambda_{ex} = 457 - 487$  nm,  $\lambda_{em} = 502 - 538$  nm), using a 40 $\times$  objective (NA = 0.6), which provides a spatial resolution of 97 nm/pixel. Images are collected using a 8-bit Point Grey Chameleon USB camera using a 100 ms exposure time, 10 Hz frame rate, and 960 pixel  $\times$  960 pixel frame size.

In this experiment, the limited resolution of fluorescence microscopy relative to the particle size precludes identification of individual particles by MPT (see Fig. 6a, inset), and thus prevents MPT analysis. Despite the lack of particle-level information, DDM is nevertheless capable of detecting the minute differences in image intensities due to particle motion, and recovers the correct diffusive dynamics (Fig. 6a). Thus, DDM shows extraordinary sensitivity even when the particle size is below the diffraction limit of the microscope.

The reference value of the MSD determined by the Stokes-Einstein relation [46] is reported by the solid black line. We generally find quantitative agreement by both DDM and DDM-UQ over most of the measured lag times, with noticeable deviations from the linear trend and the expected values at the smallest  $\Delta t$  (Fig. 6). DDM-UQ (blue diamonds), which uses an independently measured estimate of  $\sigma_0^2$ , better approximates the noise, and therefore leads to more accurate estimates of the MSD to smaller values of  $\Delta t$ . However, the measured value of  $\sigma_0^2$  appears to overestimate  $B$ , given the observed deviation from the reference value, consistent with the trends shown in Figs. 2 and 4. In the future, computational and experimental methods to further refine the estimate of  $\sigma_0^2$  will be explored. Finally, our DDM-UQ algorithm can access a larger range of  $\Delta t$  values, with a maximum measurable time lag of  $\Delta t_{max} = 3.4$ s, while the DDM algorithm only reports a lag times up to  $\Delta t_{max} = 0.7$ s.

##### C. Viscoelastic fluid

We next investigate the performance of DDM in probing the dynamics of a non-Newtonian fluid; namely, a viscoelastic worm-like micelle solution of 12.5 mM sodium salicylate (NaSal; Sigma-Aldrich, St. Louis, MO) and 15 mM cetylpyridinium chloride (CPyCl; Sigma-Aldrich, St. Louis, MO) that forms an entangled network. To this solution, fluorescent polystyrene microspheres of diameter  $2a = 1500$  nm (carboxylated yellow-green ex/em = 505/515, Life Technologies, Carlsbad, CA) are added at a volume fraction  $\phi \approx 2 \times 10^{-4}$ . The sample is mixed and allowed to relax overnight prior to loading into a capillary tube, which is sealed on both sides with optical glue (Norland Products, Inc.) and cured under a UV lamp.

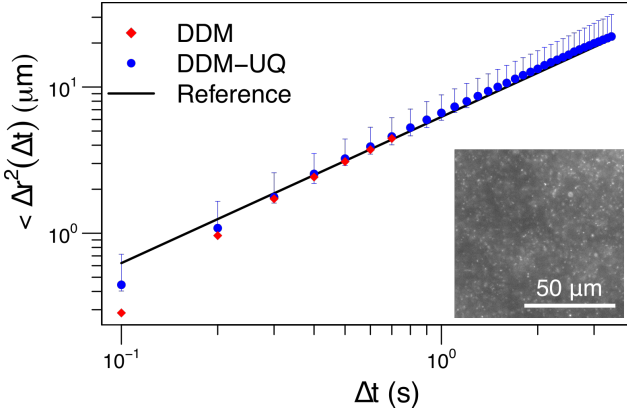


FIG. 6. Mean squared displacement estimated from the motions of 100-nm diameter probe particles in a 30% sucrose solution, which serves as a model Newtonian fluid. Red symbols denote results obtained using the conventional DDM algorithm, and blue symbols denote results obtained using the DDM-UQ analysis using only 1% of the data and informed by GPR. The black solid line denotes reference values. The inset shows a single experimental image of the movie, where particles appear to be grainy and cannot be individually resolved.

We note that this sample is similar in composition, but not identical, to a solution characterized by DDM microrheology in previous work [6]. The sample is imaged using a Zeiss Axio Observer 7 microscope in fluorescence mode using a Colibri 7 light source, standard GFP filter sets and a  $40\times$  water-immersion objective lens ( $\text{NA} = 1.2$ ), which provides a magnification of 150 nm/pixel. Images were recorded with an Axiocam 702 monochromatic camera using 15 ms exposure time, 10 Hz frame rate, and  $512 \text{ pixels} \times 512 \text{ pixels}$  frame size. In this case, the reference data set is obtained by a bulk rheology measurement of an identical sample without tracer particles using an AR-G2 stress-controlled rheometer (TA Instruments, New Castle, DE) to perform a frequency-sweep in the linear viscoelastic limit using a 40-mm diameter cone-and plate fixture, with a  $2^\circ$  cone angle and a  $55 \mu\text{m}$  truncation, at 2% shear strain over a frequency range of 0.01 - 10 rad/s. The instrument is outfitted with a solvent trap to minimize evaporation during testing.

Wormlike micelles (WLMs) manifest complex frequency-dependent viscoelasticity that nonetheless follow simple scaling laws [6, 47]. Such a system is challenging to characterize: small probe displacements at low  $\Delta t$  make it difficult to determine if the flattening of the MSD at low  $\Delta t$  is characteristic of system behavior or a result of “pixel biasing” due to particle localization error [12]. In this case, solid-like behavior at high-frequency (low  $\Delta t$ ) is confirmed by bulk rheometry measurements (Fig. 7b-d) and thus a “flattening” of the MSD trace is expected at small  $\Delta t$ . With this information, we evaluate the three methods. DDM-UQ takes into account an independently measured  $\sigma_0^2$ , and thus improves the measurements at small  $\Delta t$  over DDM,

though it is still not as accurate as MPT. The MSD trace for DDM-UQ further approaches the MPT result compared to DDM, and is more consistent with the Maxwell fluid like behavior (Fig. 7a).

In this case, we convert the measured MSD data into measures of the frequency-dependent viscoelastic moduli using the Generalized Stokes Einstein Relation (GSER) [48]:

$$|G^*(\omega)| \approx \frac{k_B T}{\pi a \langle \Delta r^2(1/\omega) \rangle \Gamma[1 + \alpha(\omega)]}, \quad (27)$$

where  $T$  is the temperature,  $k_B$  is the Boltzmann constant, and  $\alpha(\omega)$  the power-law slope (on a log-log plot of  $\langle \Delta r^2(\Delta t) \rangle$ ). The procedure of determining the power law slope  $\alpha(\omega)$  usually involves first taking the numerical derivative of  $\langle \Delta r^2(\Delta t) \rangle$  with respect to  $\Delta t$ , and then fitting a polynomial of the data around a particular  $\Delta t$ , which is then Laplace transformed to frequency space [48]. The moduli measured directly by bulk rheology generally agree with those computed from  $\langle \Delta r^2(\Delta t) \rangle$  using microrheology approaches, even at high frequency, in both magnitude and in the frequency of the crossover, as shown in Fig. 7b-d. The result from DDM is shown in red diamonds (panel b), the result using DDM-UQ is shown in blue circles (panel c), and MPT is shown in golden squares (panel c).

Both shape and magnitude of the moduli are extremely sensitive to the MSD at low  $\Delta t$ . Nevertheless, among the three methods, MPT shows the best agreement with the values obtained with macroscale rheology at higher frequencies. We note here that the numerical differentiation of  $\langle \Delta r^2(\Delta t) \rangle$  introduces a high degree of uncertainty into the moduli that is not represented on Fig. 7. To estimate the MSD for small  $\Delta t$ , the accuracy of MPT is affected by static error at each time point; thus imaging artifacts only affect position determinations for each frame. By contrast, in DDM and DDM-UQ, the error must be determined globally and effects such as bleaching and intensity fluctuations are propagated through the entire image series. Nevertheless, DDM-UQ improves the estimates of the MSD at small  $\Delta t$  by independently measuring the noise term and better isolating the signal from the noise. The development of more robust estimation methods for the moduli is an area of future research.

#### D. Model fitting for actively-driven systems

Beyond thermally-driven dynamics and microrheology, DDM can be applied in the realm of non-Brownian, active systems where models of  $f(q, \Delta t)$  can provide insight into the physics associated with the system dynamics. In such cases, the time-variation of the image structure function does not arise from probe motion but from structural evolution of actively-powered components within the system such as migrating bacteria [8] or advection due to internal stresses that arise from phase separation and aging [9], among other examples. Here we demonstrate that



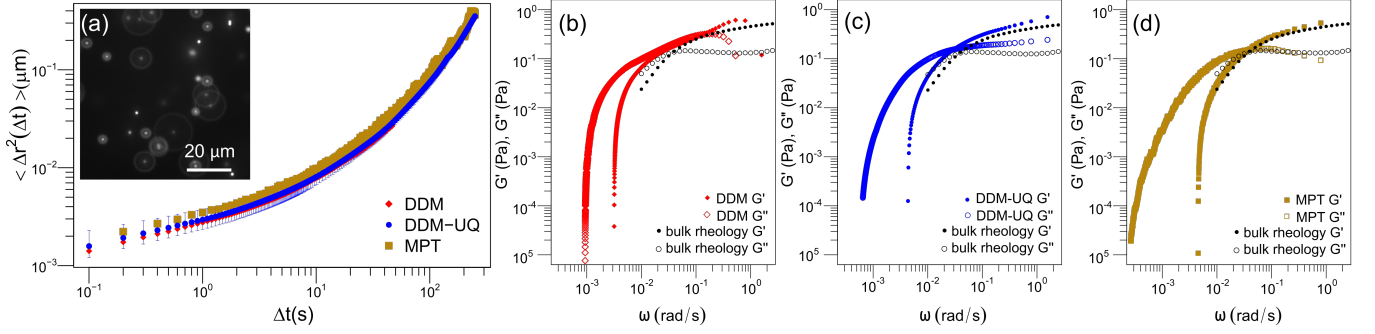


FIG. 7. Results of microrheology and bulk rheology measurements of solutions worm-like micelles, which form viscoelastic fluids. (a) Mean squared displacements obtained from the same image stack using DDM (red diamonds), DDM-UQ (blue circles) and MPT (golden squares). The inset shows an experimental snapshot of the microrheology experiment. (b-d) Comparison of the frequency-dependent linear viscoelastic moduli obtained either from bulk rheology experiments (black symbols) or calculated from the MSDs obtained by either using (b) DDM (red diamonds), (c) DDM-UQ (blue circles), or (d) MPT (golden squares). Solid symbols denote storage (elastic,  $G'(\omega)$ ) modulus while open symbols denote loss (viscous,  $G''(\omega)$ ) modulus.

DDM-UQ can be applied to such anomalous dynamics as well. Specifically, the statistical approach we have developed should be applicable to any system that sufficiently decorrelates over the experimental observation time, thus greatly simplifying the analysis and increasing the robustness of model fits.

As an example, we consider the dynamics of actively-driven composite cytoskeletal networks of actin and microtubules, by (re)analyzing the experimental data recently reported by Lee et al. [45]. Actin and microtubules are ubiquitous and essential in eukaryotic cells, and *in vitro* networks of the purified filamentous proteins are widely studied for their potential to self-organize and form model non-equilibrium materials when acted upon by ATP-driven molecular motors such as myosin. In recent work, Lee et al. [45] investigated a composite network comprising actin and microtubules, which were each labeled with distinct fluorophores, and acted upon by myosin. DDM was then used as a means of disentangling the motions recorded through the individual fluorescence channels, allowing investigation of the mechanisms of cross-correlation of actin and microtubule dynamics within the entangled network. By contrast, MPT can provide only information on the bulk network itself.

The dynamics of such an active system can be described by a stretched exponential model [45]:

$$f(q, \Delta t) = \exp \left( - \left( \frac{\Delta t}{\tau(q)} \right)^{\gamma(q)} \right), \quad (28)$$

where  $\gamma(q) > 1$  means the system shows contractile dynamics, while  $\gamma(q) < 1$  when the system shows stretching dynamics. A relaxation time scaling where  $\tau(q) = \frac{1}{vq}$  describes a system exhibiting ballistic motion with velocity  $v$ , whereas  $\tau(q) = \frac{1}{D_m q^2}$  describes a system exhibiting diffusive motion where  $D_m$  represents the diffusion coefficient.

Given the intrinsically heterogeneous nature of such

systems, multiple replicates of the same composition are often examined, increasing the already heavy computational costs that are typical of DDM analysis. Here we speed up computation by only computing a fraction of the image structure function. To demonstrate this, we re-analyze six replicates of the active actin data set from [45] to show that despite using only 1% of the data, DDM-UQ can extract essentially the same information with the same confidence intervals as the DDM approach originally employed. In detail, the full  $D_o(q, \Delta t)$  is computed directly from the image stacks by DDM, from which a subset of values (around 1%),  $D_o(q, \Delta t)$  are pre-selected to obtain the predictive distribution by DDM-UQ. The imaging noise is estimated using a movie of an inactive network taken under similar imaging conditions. The inactive network contains no myosin motor proteins, and thus is nearly static on the timescale of the experiment.

Previously, this dataset was analyzed by DDM to show that it does not reach a decorrelation plateau [45]. When a stretched exponential model (Eq. 28) for  $f(q, \Delta t)$  with coefficients  $\tau(q)$  and  $\gamma(q)$ , along with  $A(q)$  and  $B(q)$ , is fit to either the full matrix  $D_o(q, \Delta t)$  (DDM) or the predictive distribution  $D(q, \Delta t)$  (DDM-UQ), the estimated image structure function  $D_e(q, \Delta t)$  is obtained.  $D(q, \Delta t)$  contains the same number of entries as  $D_o(q, \Delta t)$ ; it is reconstructed using the mean of values sampled from the predictive distribution  $D(q, \Delta t)$  (300 instances at every  $(q, \Delta t)$ ). The purpose of this step is to extract coefficients  $\tau(q)$  and  $\gamma(q)$  relevant to the underlying physical process. The difference between the estimated quantity  $D_e(q, \Delta t)$  from fitting stretched exponential model, and observed quantity  $D_o(q, \Delta t)$  is evaluated by the N-RMSE:

$$\text{N-RMSE} = \frac{\sqrt{\frac{1}{n_q n_{\Delta t}} \sum_{\Delta t \in \Delta \mathcal{T}} \sum_{q \in \mathcal{Q}} (\langle \tilde{D}_o(q, \Delta t) \rangle - \langle \tilde{D}_e(q, \Delta t) \rangle)^2}}{\tilde{\sigma}_D}, \quad (29)$$

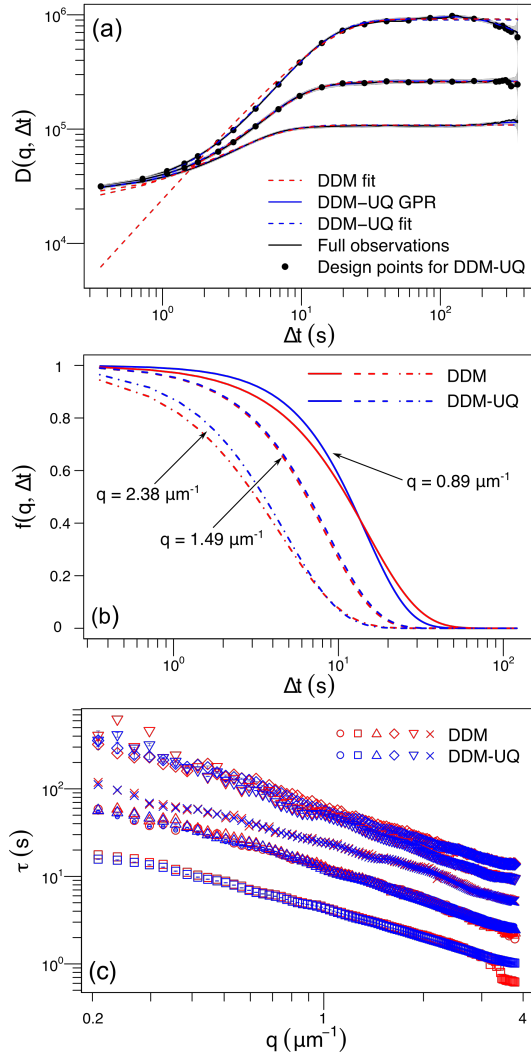


FIG. 8. Example of analysis of an actively-driven system. Experimental data extracted from a fluorescently-labeled actin-myosin-microtubule composite network system reported in [45], processed using DDM (red symbols) or DDM-UQ (blue symbols), and fit to a stretched exponential model to describe the system dynamics (Eq. (28)). (a) Comparing DDM, and DDM DQ fits to the original  $D_o(q, \Delta t)$  matrix, where the uncertainty is denoted by the grey shaded area, which is very small as the uncertainty is low. The solid line denotes full  $D_o(q, \Delta t)$  data, while the solid dots denotes  $D_o(q, \Delta t)$  selected to obtain the predictive distribution. (b) Fits to  $f(q, \Delta t)$  shown at several different  $q$ 's. (c) Parameter  $\tau$ , which describes the system relaxation time, plotted as a function of  $q$ . Different symbols represent  $\tau$  extracted from 6 different data sets. From this, the system velocity is obtained (Fig. 9).

where  $\tilde{D}_o(q, t)$  and  $\tilde{D}_e(q, \Delta t)$  are the logarithm of the observed and estimated image structure function by different approaches, and  $\tilde{\sigma}_D$  is the logarithm of sample standard deviation;  $\Delta\mathcal{T}$  and  $\mathcal{Q}$  are the sets of  $\Delta t$  and  $q$  available for comparison, respectively.

Figure 8a shows reconstructed  $D(q, \Delta t)$  (dashed lines) from fitting the full observation (solid line) using DDM as

TABLE II. N-RMSE of active actin networks

Sample ID	<70% Plateau		Full Data	
	DDM	DDM-UQ	DDM	DDM-UQ
1	0.190	0.036	0.371	0.334
2	0.232	0.028	0.618	0.600
3	0.099	0.022	0.237	0.231
4	0.148	0.092	0.209	0.223
5	0.142	0.064	0.205	0.201
6	0.225	0.076	0.241	0.230

well as a reconstructed  $D(q, \Delta t)$  obtained by resampling with only a fraction of design points (black dots) using DDM-UQ. There is general agreement between the two approaches at all  $q$  values, with some differences observed at short times because DDM-UQ weighs more heavily data at small  $\Delta t$ , since the number of pixels used to obtain  $f(q, \Delta t)$  at small  $\Delta t$  is large. Because DDM applies a uniform weight across all  $\Delta t$ , the DDM fit deviates in the limit of small  $\Delta t$ , as previously observed [8]. Similar differences are seen in Fig. 8b: here, the same fits of the stretched exponential model are used to reconstruct  $f(q, \Delta t)$  at different  $q$ 's using the full observed ISF  $D_o(q, \Delta t)$  obtained by conventional DDM (red lines) and based on 1% of  $D_o(q, \Delta t)$  using DDM-UQ (blue lines). Note that DDM-UQ only uses observations  $D_o(q, \Delta t)$  at selected  $q$  and  $\Delta t$ , but it performs equally well even for unobserved  $q$  values for which there is no observation for any  $\Delta t$  (see Fig. 8a, bottom curve).

The differences between the estimated and observed values of  $D_o(q, \Delta t)$  for DDM and DDM-UQ are quantified by the N-RMSE in Eq. (29) as shown in Table II. Since  $D(q, \Delta t)$  at large  $\Delta t$  contains fewer independent samples and shows large fluctuations, it is informative to compare the accuracy of the fit only up to a threshold value, chosen here to be 70% of the  $\Delta t$  values before the plateau is reached. In all cases, DDM-UQ outperforms DDM in more closely approximating the  $D_o(q, \Delta t)$  when comparing the truncated dataset, and in almost all cases, the fit of DDM-UQ which uses only 1% of the data is comparable to that of DDM when the full data resolution is used, as shown in Figure II. Thus, DDM-UQ significantly accelerates the analysis without any observable sacrifice in accuracy with respect to post-processing of the data such as model fitting.

As described in Eq. (28),  $f(q, \Delta t)$  contains the fit parameters  $\gamma(q)$  and  $\tau(q)$ . Following [45], we fit the data to a linear model  $\tau(q) = \frac{1}{vq}$  and extract the characteristic velocities of the active actin mixture (Fig. 8c). The maximum likelihood estimator (MLE) and the confidence interval (CI) for the velocities from different replicates are tabulated in Figure 9. Importantly, DDM-UQ with its limited observations largely recovers similar characteristic velocities and confidence intervals as those obtained using the full matrix, paving the way for high-throughput analysis of the dynamic properties of complex biomaterial systems.



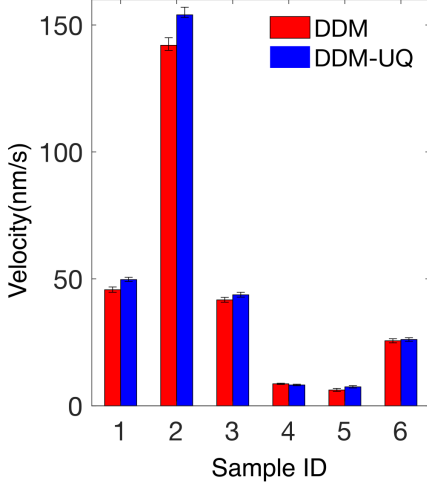


FIG. 9. Velocity estimates and confidence intervals extracted from fitting the stretched exponential model to either the full observations (DDM) or to reconstructed  $D(q, \Delta t)$  from selected design points (DDM-UQ). The error bars denote 95% confidence intervals.

## V. CONCLUDING REMARKS

DDM can be applied to a structurally evolving image stack to obtain the image structure function and intermediate scattering function. It provides an ensemble-averaged measure of dynamics, potentially offering higher sensitivity than using real-space data alone. When combined with models of  $f(q, \Delta t)$ , DDM also provides a powerful approach in extracting physical quantities of interest. While the theoretical framework of DDM is well established, to our knowledge, this paper represents the first exploration into how to quantify and propagate the uncertainty associated with measurement noise in the image intensity. Based on error propagation in estimating the image structure function, we derived an unbiased estimator of the mean of the noise term  $B$ , leading to more accurate estimation of the ISF and MSD at small  $\Delta t$ . Moreover, we showed that when a small subset of  $D_o(q, \Delta t)$  (around 1%) at selected  $q$  and  $\Delta t$  were used to obtain predictive median and samples in GPR, the image structure function at unobserved inputs and subsequent

quantities of interest could be robustly predicted. Both simulations and experiments were presented to demonstrate that our method has virtually no loss of information, while reducing the computational order by 100-fold. The combination of error propagation and GPR results in more robust determination of  $D(q, \Delta t)$  at long times and small  $q$ -values, providing further improvements to the determination of the ISF and MSD.

We anticipate that these results will enable many new applications of DDM to complex biomaterial and soft material systems [49, 50]. With the potential to carry out real-time analysis via down-sampling, the proposed method can be extended to map out an entire phase space of material composition or physicochemical conditions in a high-throughput manner. This increased performance also places new demands on the general applicability of the algorithm, for instance, to provide meaningful analysis of stiffer materials that do not fully decorrelate as quickly as a more fluid-like samples, as well as heterogeneous samples, through analysis of sub-populations that demonstrate distinct features. Another potential innovation includes estimating the imaging noise  $\sigma_0^2$  from the same imaging stack used to extract dynamics. These will be pursued in future work.

## ACKNOWLEDGEMENTS

This work was supported by the BioPACIFIC Materials Innovation Platform of the National Science Foundation under Award No. DMR-1933487 (NSF BioPACIFIC MIP), with partial support by the Materials Research Science and Engineering Center (MRSEC) Program of the National Science Foundation under Award No. DMR-1720256 (IRG-3). MEH acknowledges partial support from the National Science Foundation under Award No. CBET-1729108. This work used computational facilities purchased with funds from the National Science Foundation (CNS-1725797) and administered by the Center for Scientific Computing (CSC). The CSC is supported by the California NanoSystems Institute and MRSEC (NSF DMR-1720256) at UC Santa Barbara. We thank Gloria Lee and Rae Robertson-Anderson from University of San Diego for providing the the active actin dataset.

---

[1] J. C. Crocker and D. G. Grier, Methods of digital video microscopy for colloidal studies, *J. Colloid Interface Sci.* **179**, 298 (1996).  
[2] T. Savin and P. S. Doyle, Statistical and sampling issues when using multiple particle tracking, *Phys. Rev. E* **76**, 021501 (2007).  
[3] F. Giavazzi, D. Brogioli, V. Trappe, T. Bellini, and R. Cerbino, Scattering information obtained by optical microscopy: differential dynamic microscopy and be-

yond, *Phys. Rev. E* **80**, 031403 (2009).  
[4] F. Giavazzi and R. Cerbino, Digital Fourier microscopy for soft matter dynamics, *J. Opt.* **16**, 083001 (2014).  
[5] R. Cerbino and V. Trappe, Differential dynamic microscopy: probing wave vector dependent dynamics with a microscope, *Phys. Rev. Lett.* **100**, 188102 (2008).  
[6] A. V. Bayles, T. M. Squires, and M. E. Helgeson, Probe microrheology without particle tracking by differential dynamic microscopy, *Rheol. Acta* **56**, 863 (2017).

- [7] P. J. Lu, F. Giavazzi, T. E. Angelini, E. Zaccarelli, F. Jargstorff, A. B. Schofield, J. N. Wilking, M. B. Romanowsky, D. A. Weitz, and R. Cerbino, Characterizing concentrated, multiply scattering, and actively driven fluorescent systems with confocal differential dynamic microscopy, *Phys. Rev. Lett.* **108**, 218103 (2012).
- [8] V. A. Martinez, R. Besseling, O. A. Croze, J. Tailleur, M. Reufer, J. Schwarz-Linek, L. G. Wilson, M. A. Bees, and W. C. Poon, Differential dynamic microscopy: A high-throughput method for characterizing the motility of microorganisms, *Biophys. J.* **103**, 1637 (2012).
- [9] Y. Gao, J. Kim, and M. E. Helgeson, Microdynamics and arrest of coarsening during spinodal decomposition in thermoreversible colloidal gels, *Soft Matter* **11**, 6360 (2015).
- [10] F. Giavazzi, S. Crotti, A. Speciale, F. Serra, G. Zanchetta, V. Trappe, M. Buscaglia, T. Bellini, and R. Cerbino, Viscoelasticity of nematic liquid crystals at a glance, *Soft Matter* **10**, 3938 (2014).
- [11] R. Cerbino and P. Cicuta, Perspective: Differential dynamic microscopy extracts multi-scale activity in complex fluids and biological systems, *J. Chem. Phys.* **147**, 110901 (2017).
- [12] T. Savin and P. S. Doyle, Static and dynamic errors in particle tracking microrheology, *Biophys. J.* **88**, 623 (2005).
- [13] M. Reufer, V. A. Martinez, P. Schurtenberger, and W. C. Poon, Differential dynamic microscopy for anisotropic colloidal dynamics, *Langmuir* **28**, 4618 (2012).
- [14] C. Kurzthaler, C. Devailly, J. Arlt, T. Franosch, W. C. Poon, V. A. Martinez, and A. T. Brown, Probing the spatiotemporal dynamics of catalytic janus particles with single-particle tracking and differential dynamic microscopy, *Phys. Rev. Lett.* **121**, 078001 (2018).
- [15] K. Regan, D. Wulstein, H. Rasmussen, R. McGorty, and R. M. Robertson-Anderson, Bridging the spatiotemporal scales of macromolecular transport in crowded biomimetic systems, *Soft matter* **15**, 1200 (2019).
- [16] L. Feriani, M. Juenet, C. J. Fowler, N. Bruot, M. Chioccioli, S. M. Holland, C. E. Bryant, and P. Cicuta, Assessing the collective dynamics of motile cilia in cultures of human airway cells by multiscale DDM, *Biophys. J.* **113**, 109 (2017).
- [17] M. Norouziadeh, G. Cerchiari, and F. Croccolo, Increased performance in DDM analysis by calculating structure functions through Fourier transform in time, *arXiv preprint arXiv:2012.05695* (2020).
- [18] P. Edera, D. Bergamini, V. Trappe, F. Giavazzi, and R. Cerbino, Differential dynamic microscopy microrheology of soft materials: A tracking-free determination of the frequency-dependent loss and storage moduli, *Phys. Rev. Materials* **1**, 073804 (2017).
- [19] T. G. Mason, K. Ganesan, J. H. van Zanten, D. Wirtz, and S. C. Kuo, Particle tracking microrheology of complex fluids, *Phys. Rev. Lett.* **79**, 3282 (1997).
- [20] T. G. Mason and D. A. Weitz, Optical measurements of frequency-dependent linear viscoelastic moduli of complex fluids, *Phys. Rev. Lett.* **74**, 1250 (1995).
- [21] R. Cerbino, D. Piotti, M. Buscaglia, and F. Giavazzi, Dark field differential dynamic microscopy enables accurate characterization of the roto-translational dynamics of bacteria and colloidal clusters, *J. Phys. Condens. Matter* **30**, 025901 (2017).
- [22] M. S. Safari, M. A. Vorontsova, R. Poling-Skutvik, P. G. Vekilov, and J. C. Conrad, Differential dynamic microscopy of weakly scattering and polydisperse protein-rich clusters, *Phys. Rev. E* **92**, 042712 (2015).
- [23] T. Sentjabrskaja, E. Zaccarelli, C. De Michele, F. Sciortino, P. Tartaglia, T. Voigtmann, S. U. Egelhaaf, and M. Laurati, Anomalous dynamics of intruders in a crowded environment of mobile obstacles, *Nat. Comm.* **7**, 1 (2016).
- [24] C. E. Rasmussen, *Gaussian processes for machine learning* (MIT Press, 2006).
- [25] F. Giavazzi, P. Edera, P. J. Lu, and R. Cerbino, Image windowing mitigates edge effects in differential dynamic microscopy, *Eur. Phys. J. E* **40**, 97 (2017).
- [26] B. Nijboer and A. Rahman, Time expansion of correlation functions and the theory of slow neutron scattering, *Physica* **32**, 415 (1966).
- [27] E. R. Weeks, J. C. Crocker, A. C. Levitt, A. Schofield, and D. A. Weitz, Three-dimensional direct imaging of structural relaxation near the colloidal glass transition, *Science* **287**, 627 (2000).
- [28] L. Jawerth, E. Fischer-Friedrich, S. Saha, J. Wang, T. Franzmann, X. Zhang, J. Sachweh, M. Ruer, M. Ijavi, S. Saha, *et al.*, Protein condensates as aging Maxwell fluids, *Science* **370**, 1317 (2020).
- [29] E. M. Furst and T. M. Squires, *Microrheology* (Oxford University Press, 2017).
- [30] J. A. McGlynn, N. Wu, and K. M. Schultz, Multiple particle tracking microrheological characterization: Fundamentals, emerging techniques and applications, *Journal of Applied Physics* **127**, 201101 (2020).
- [31] M. Gu, J. Palomo, and J. O. Berger, RobustGaSP: Robust Gaussian Stochastic Process Emulation in R, *The R Journal* **11**, 112 (2019).
- [32] M. Gu, X. Wang, and J. O. Berger, Robust Gaussian stochastic process emulation, *The Annals of Statistics* **46**, 3038 (2018).
- [33] M. Rupp, A. Tkatchenko, K.-R. Müller, and O. A. Von Lilienfeld, Fast and accurate modeling of molecular atomization energies with machine learning, *Physical review letters* **108**, 058301 (2012).
- [34] A. P. Bartók, R. Kondor, and G. Csányi, On representing chemical environments, *Phys. Rev. B* **87**, 184115 (2013).
- [35] S. Chmiela, A. Tkatchenko, H. E. Sauceda, I. Poltavsky, K. T. Schütt, and K.-R. Müller, Machine learning of accurate energy-conserving molecular force fields, *Sci. Adv.* **3**, e1603015 (2017).
- [36] F. Brockherde, L. Vogt, L. Li, M. E. Tuckerman, K. Burke, and K.-R. Müller, Bypassing the kohn-sham equations with machine learning, *Nat. Comm.* **8**, 1 (2017).
- [37] S. Chmiela, H. E. Sauceda, K.-R. Müller, and A. Tkatchenko, Towards exact molecular dynamics simulations with machine-learned force fields, *Nat. Comm.* **9**, 1 (2018).
- [38] A. P. Bartók, J. Kermode, N. Bernstein, and G. Csányi, Machine learning a general-purpose interatomic potential for silicon, *Phys. Rev. X* **8**, 041048 (2018).
- [39] D. M. Wilkins, A. Grisafi, Y. Yang, K. U. Lao, R. A. DiStasio, and M. Ceriotti, Accurate molecular polarizabilities with coupled cluster theory and machine learning, *Proc. Natl. Acad. Sci. U.S.A.* **116**, 3401 (2019).
- [40] K. R. Anderson, I. A. Johanson, M. R. Patrick, M. Gu, P. Segall, M. P. Poland, E. K. Montgomery-Brown, and

- A. Miklius, Magma reservoir failure and the onset of caldera collapse at Kilauea volcano in 2018, *Science* **366** (2019).
- [41] J. Wu and M. Gu, Emulating the first principles of mmatter: a probabilistic roadmap, arXiv preprint arXiv:2010.05942 (2020).
- [42] Y. Gao and M. L. Kilfoil, Accurate detection and complete tracking of large populations of features in three dimensions, *Opt. Exp.* **17**, 4685 (2009).
- [43] J.-Z. Xue, D. Pine, S. T. Milner, X.-L. Wu, and P. Chaikin, Nonergodicity and light scattering from polymer gels, *Phys. Rev. A* **46**, 6550 (1992).
- [44] N. Monnier, S.-M. Guo, M. Mori, J. He, P. Lénárt, and M. Bathe, Bayesian approach to MSD-based analysis of particle motion in live cells, *Biophys. J.* **103**, 616 (2012).
- [45] G. Lee, G. Leech, M. J. Rust, M. Das, R. J. McGorty, J. L. Ross, and R. M. Robertson-Anderson, Myosin-driven actin-microtubule networks exhibit self-organized contractile dynamics, *Sci. Adv.* **7**, eabe4334 (2021).
- [46] A. V. Bayles, T. M. Squires, and M. E. Helgeson, Dark-field differential dynamic microscopy, *Soft Matter* **12**, 2440 (2016).
- [47] H. Rehage and H. Hoffmann, Viscoelastic surfactant solutions: model systems for rheological research, *Mol. Phys.* **74**, 933 (1991).
- [48] T. G. Mason, Estimating the viscoelastic moduli of complex fluids using the generalized Stokes–Einstein equation, *Rheol. Acta* **39**, 371 (2000).
- [49] J. Fricks, L. Yao, T. C. Elston, and M. G. Forest, Time-domain methods for diffusive transport in soft matter, *SIAM J. Appl. Math.* **69**, 1277 (2009).
- [50] M. Lysy, N. S. Pillai, D. B. Hill, M. G. Forest, J. W. Melnik, P. A. Vasquez, and S. A. McKinley, Model comparison and assessment for single particle tracking in biological fluids, *J. Am. Stat. Assoc.* **111**, 1413 (2016).

## APPENDICES

### APPENDIX A

*Proof of Eq. (6) and Eq. (7).* The observed difference of the intensity at two time points ( $t + \Delta t$ ) and  $t$  can be described as

$$\Delta I_o(\mathbf{x}, t, \Delta t) = \Delta I(\mathbf{x}, t, \Delta t) + \Delta \epsilon(\mathbf{x}, t, \Delta t),$$

where  $\Delta I(\mathbf{x}, t, \Delta t) = I(\mathbf{x}, t + \Delta t) - I(\mathbf{x}, t)$  and  $\Delta \epsilon(\mathbf{x}, t, \Delta t) = \epsilon(\mathbf{x}, t + \Delta t) - \epsilon(\mathbf{x}, t)$ . We denote the minimum time interval by  $\Delta t_{\min} = 1$  and  $\Delta t = l\Delta t_{\min} = l$ , where  $l$  is a positive integer smaller than  $T$ .

We apply 2D discrete Fourier transformations on  $\Delta I_o(\mathbf{x}, t, \Delta t)$  and obtain

$$\begin{aligned} & |\Delta \hat{I}_o(\mathbf{q}, t, \Delta t)|^2 \\ &= \frac{1}{N^2} \sum_{x_1=0}^{N-1} \sum_{x_2=0}^{N-1} \Delta I_o(\mathbf{x}, t, \Delta t) \left| \exp\left(-\frac{i2\pi \mathbf{x}^T \mathbf{q}}{N}\right) \right|^2 \\ &= \frac{1}{N^2} \sum_{x_1=0}^{N-1} \sum_{x_2=0}^{N-1} \Delta I_o(\mathbf{x}, t, \Delta t) \left\{ \cos\left(\frac{2\pi \mathbf{x}^T \mathbf{q}}{N}\right) \right\}^2 \\ &\quad + \frac{1}{N^2} \sum_{x_1=0}^{N-1} \sum_{x_2=0}^{N-1} \Delta I_o(\mathbf{x}, t, \Delta t) \left\{ \sin\left(\frac{2\pi \mathbf{x}^T \mathbf{q}}{N}\right) \right\}^2 \\ &:= \Delta \hat{I}_{o,1}^2(\mathbf{q}, t, \Delta t) + \Delta \hat{I}_{o,2}^2(\mathbf{q}, t, \Delta t) \end{aligned}$$

where  $\hat{I}_{o,1}(\mathbf{q}, t, \Delta t)$  and  $\hat{I}_{o,2}(\mathbf{q}, t, \Delta t)$  are independent from each other by the orthogonality of the Fourier basis with

$$\begin{aligned} \mathbb{E}[\hat{I}_{o,1}(\mathbf{q}, t, \Delta t)] &= \frac{1}{N} \sum_{x_1=0}^{N-1} \sum_{x_2=0}^{N-1} \Delta I(\mathbf{x}, t, \Delta t) \cos\left(\frac{2\pi \mathbf{x}^T \mathbf{q}}{N}\right) \\ \mathbb{E}[\hat{I}_{o,2}(\mathbf{q}, t, \Delta t)] &= \frac{1}{N} \sum_{x_1=0}^{N-1} \sum_{x_2=0}^{N-1} \Delta I(\mathbf{x}, t, \Delta t) \sin\left(\frac{2\pi \mathbf{x}^T \mathbf{q}}{N}\right) \\ \mathbb{V}[\hat{I}_{o,1}(\mathbf{q}, t, \Delta t)] &= \mathbb{V}[\hat{I}_{o,2}(\mathbf{q}, t, \Delta t)] = \sigma_0^2 \end{aligned}$$

Furthermore

$$\begin{aligned} & |\Delta \hat{I}_o(\mathbf{q}, t, \Delta t)|^2 \\ &= |\Delta \hat{I}(\mathbf{q}, t, \Delta t)|^2 + 2\Delta \hat{I}(\mathbf{q}, t, \Delta t)\Delta \hat{\epsilon}(\mathbf{q}, t, \Delta t) + |\Delta \hat{\epsilon}(\mathbf{q}, t, \Delta t)|^2 \end{aligned}$$

where

$$|\Delta \hat{I}(\mathbf{q}, t, \Delta t)|^2 = \Delta \hat{I}_1^2 + \Delta \hat{I}_2^2, \quad (30)$$

$$\Delta \hat{I}(\mathbf{q}, t, \Delta t)\Delta \hat{\epsilon}(\mathbf{q}, t, \Delta t) = \Delta \hat{I}_1\epsilon_1 + \Delta \hat{I}_2\epsilon_2, \quad (31)$$

$$|\Delta \hat{\epsilon}(\mathbf{q}, t, \Delta t)|^2 = \Delta \hat{\epsilon}_1^2 + \Delta \hat{\epsilon}_2^2 \quad (32)$$

with

$$\begin{aligned} \Delta \hat{I}_1 &= \frac{1}{N} \sum_{x_1=0}^{N-1} \sum_{x_2=0}^{N-1} \Delta I(\mathbf{x}, t, \Delta t) \cos\left(\frac{2\pi \mathbf{x}^T \mathbf{q}}{N}\right) \\ \Delta \hat{\epsilon}_1 &= \frac{1}{N} \sum_{x_1=0}^{N-1} \sum_{x_2=0}^{N-1} \Delta \epsilon(\mathbf{x}, t, \Delta t) \cos\left(\frac{2\pi \mathbf{x}^T \mathbf{q}}{N}\right) \\ \Delta \hat{I}_2 &= \frac{1}{N} \sum_{x_1=0}^{N-1} \sum_{x_2=0}^{N-1} \Delta I(\mathbf{x}, t, \Delta t) \sin\left(\frac{2\pi \mathbf{x}^T \mathbf{q}}{N}\right) \\ \Delta \hat{\epsilon}_2 &= \frac{1}{N} \sum_{x_1=0}^{N-1} \sum_{x_2=0}^{N-1} \Delta \epsilon(\mathbf{x}, t, \Delta t) \sin\left(\frac{2\pi \mathbf{x}^T \mathbf{q}}{N}\right). \end{aligned}$$

The expected value of  $\mathbb{E}[|\hat{I}_o(\mathbf{q}, t, \Delta t)|^2]$  can be verified using properties of the Fourier basis.  $\square$

*Proof of Eq. (8) - Eq. (10).* The observations of image structure function can be obtained through computing ensemble average of the observed intensity

$$\begin{aligned} D_o(q, \Delta t) &= \langle |\Delta \hat{I}_o(\mathbf{q}, t, \Delta t)|^2 \rangle \\ &= \langle |\Delta \hat{I}(\mathbf{q}, t, \Delta t)|^2 \rangle + 2\langle \Delta \hat{I}(\mathbf{q}, t, \Delta t) \Delta \hat{\epsilon}(\mathbf{q}, t, \Delta t) \rangle \\ &\quad + \langle |\hat{\epsilon}(\mathbf{q}, t, \Delta t)|^2 \rangle \end{aligned}$$

with expected value and variance:

$$\begin{aligned} \mathbb{E}[D_o(q, \Delta t)] &= \mathbb{E}[\langle |\Delta \hat{I}(\mathbf{q}, t, \Delta t)|^2 \rangle] + 2\mathbb{E}[\langle \Delta \hat{I}(\mathbf{q}, t, \Delta t) \Delta \hat{\epsilon}(\mathbf{q}, t, \Delta t) \rangle] \\ &\quad + \mathbb{E}[\langle |\hat{\epsilon}(\mathbf{q}, t, \Delta t)|^2 \rangle] \\ &= \langle |\Delta \hat{I}(\mathbf{q}, t, \Delta t)|^2 \rangle \\ &\quad + \frac{2}{n_{\Delta t} n_q} \sum_{t \in \mathcal{S}_{\Delta t}} \sum_{(q_1, q_2) \in \mathcal{S}_q} \Delta \hat{I}(\mathbf{q}, t, \Delta t) \mathbb{E}[\Delta \hat{\epsilon}(\mathbf{q}, t, \Delta t)] \\ &\quad + \frac{1}{n_{\Delta t} n_q} \sum_{t \in \mathcal{S}_{\Delta t}} \sum_{(q_1, q_2) \in \mathcal{S}_q} \mathbb{E}[\Delta \hat{\epsilon}_1^2 + \Delta \hat{\epsilon}_2^2] \\ &= D(q, \Delta t) + \mathbb{V}(\Delta \hat{\epsilon}_1) + \mathbb{V}(\Delta \hat{\epsilon}_2) \\ &= D(q, \Delta t) + 2\sigma_0^2 \end{aligned}$$

where  $\langle \cdot \rangle$  denotes averaging over available time points for each  $\Delta t$ , and  $(q_1, q_2) \in \mathcal{S}_q$  with  $\mathcal{S}_q := \{(q_1, q_2) : q_1^2 + q_2^2 = q^2\}$ ,  $n_q := |\mathcal{S}_q|$  and  $n_{\Delta t} := t_{max} - \Delta t$ .

$$\begin{aligned} \mathbb{V}[D_o(q, \Delta t)] &= \mathbb{V}[\langle |\Delta \hat{I}_o(\mathbf{q}, t, \Delta t)|^2 \rangle] \\ &= \mathbb{V}\left[\frac{1}{n_q n_{\Delta t}} \sum_{(q_1, q_2) \in \mathcal{S}_q} \sum_{t \in \mathcal{S}_{\Delta t}} |\Delta \hat{I}_o(\mathbf{q}, t, \Delta t)|^2\right] \end{aligned}$$

The variance of the average of intensity over available time points for each  $\Delta t$  and  $t_{max} = T$  is

$$\begin{aligned} &\mathbb{V}\left[\frac{1}{n_{\Delta t}} \sum_{t \in \mathcal{S}_{\Delta t}} |\Delta \hat{I}_o(\mathbf{q}, t, \Delta t)|^2\right] \\ &= \mathbb{V}\left[\frac{1}{n_{\Delta t}} \sum_{t \in \mathcal{S}_{\Delta t}} (\Delta \hat{I}_{o,1}^2(\mathbf{q}, t, \Delta t) + \Delta \hat{I}_{o,2}^2(\mathbf{q}, t, \Delta t))\right] \\ &= \frac{1}{n_{\Delta t}^2} \sum_{t \in \mathcal{S}_{\Delta t}} \mathbb{V}[\Delta \hat{I}_{o,1}^2(\mathbf{q}, t, \Delta t)] \\ &\quad + \frac{1}{n_{\Delta t}^2} \sum_{t \in \mathcal{S}_{\Delta t}} \mathbb{V}[\Delta \hat{I}_{o,2}^2(\mathbf{q}, t, \Delta t)] \\ &\quad + \frac{1}{n_{\Delta t}^2} \sum_{t_1 \neq t_2} \text{Cov}(\Delta \hat{I}_{o,1}^2(\mathbf{q}, t_1, \Delta t), \Delta \hat{I}_{o,1}^2(\mathbf{q}, t_2, \Delta t)) \\ &\quad + \frac{1}{n_{\Delta t}^2} \sum_{t_1 \neq t_2} \text{Cov}(\Delta \hat{I}_{o,2}^2(\mathbf{q}, t_1, \Delta t), \Delta \hat{I}_{o,2}^2(\mathbf{q}, t_2, \Delta t)) \end{aligned}$$

where the first two terms can be computed as

$$\begin{aligned} &\frac{1}{n_{\Delta t}^2} \sum_{t \in \mathcal{S}_{\Delta t}} \left( \mathbb{V}[\Delta \hat{I}_{o,1}^2(\mathbf{q}, t, \Delta t)] + \mathbb{V}[\Delta \hat{I}_{o,2}^2(\mathbf{q}, t, \Delta t)] \right) \\ &= \frac{1}{n_{\Delta t}^2} \sum_{t=1}^{n_{\Delta t}} \left( \mathbb{V}[(\Delta \hat{I}_1 + \Delta \hat{\epsilon}_1)^2] + \mathbb{V}[(\Delta \hat{I}_2 + \Delta \hat{\epsilon}_2)^2] \right) \\ &= \frac{1}{n_{\Delta t}^2} \sum_{t=1}^{n_{\Delta t}} \left( \mathbb{V}[2\Delta \hat{I}_1 \Delta \hat{\epsilon}_1 + \Delta \hat{\epsilon}_1^2] + \mathbb{V}[2\Delta \hat{I}_2 \Delta \hat{\epsilon}_2 + \Delta \hat{\epsilon}_2^2] \right) \\ &= \frac{1}{n_{\Delta t}^2} \sum_{t=1}^{n_{\Delta t}} \left( 4\sigma_0^2(\Delta \hat{I}_1^2 + \Delta \hat{I}_2^2) + \mathbb{V}(\Delta \hat{\epsilon}_1 + \Delta \hat{\epsilon}_2) \right) \\ &= \frac{1}{n_{\Delta t}^2} \sum_{t=1}^{n_{\Delta t}} \left( 4\sigma_0^2 |\Delta \hat{I}_o(\mathbf{q}, t, \Delta t)|^2 + 4\sigma_0^4 \right), \end{aligned}$$

and for  $\Delta t = 1, 2, \dots, \lfloor (t_{max} - 1)/2 \rfloor$ , the last two terms follows:

$$\begin{aligned} &\sum_{t_1 \neq t_2} \text{Cov}(\Delta \hat{I}_{o,1}^2(\mathbf{q}, t_1, \Delta t), \Delta \hat{I}_{o,1}^2(\mathbf{q}, t_2, \Delta t)) \\ &= 2 \sum_{t=1}^{T-2\Delta t} \text{Cov}(\Delta \hat{I}_{o,1}^2(\mathbf{q}, t, \Delta t), \Delta \hat{I}_{o,1}^2(\mathbf{q}, t + \Delta t, \Delta t)) \\ &= 2 \sum_{t=1}^{T-2\Delta t} \text{Cov}((\Delta \hat{I}_1(\mathbf{q}, t, \Delta t) + \hat{\epsilon}_{1,t+\Delta t} - \hat{\epsilon}_{1,t})^2, \\ &\quad (\Delta \hat{I}_1(\mathbf{q}, t + \Delta t, \Delta t) + \hat{\epsilon}_{1,t+2\Delta t} - \hat{\epsilon}_{1,t+\Delta t})^2) \\ &= 2 \sum_{t=1}^{T-2\Delta t} \text{Cov}(\mathbb{E}[(\Delta \hat{I}_1(\mathbf{q}, t, \Delta t) + \hat{\epsilon}_{1,t+\Delta t} - \hat{\epsilon}_{1,t})^2], \\ &\quad \mathbb{E}[(\Delta \hat{I}_1(\mathbf{q}, t + \Delta t, \Delta t) + \hat{\epsilon}_{1,t+2\Delta t} - \hat{\epsilon}_{1,t+\Delta t})^2] | \hat{\epsilon}_{1,t+\Delta t}) \\ &\quad + 2 \sum_{t=1}^{T-2\Delta t} \mathbb{E}[\text{Cov}((\Delta \hat{I}_1(\mathbf{q}, t, \Delta t) + \hat{\epsilon}_{1,t+\Delta t} - \hat{\epsilon}_{1,t})^2, \\ &\quad (\Delta \hat{I}_1(\mathbf{q}, t + \Delta t, \Delta t) + \hat{\epsilon}_{1,t+2\Delta t} - \hat{\epsilon}_{1,t+\Delta t})^2 | \hat{\epsilon}_{1,t+\Delta t})] \\ &= 2 \sum_{t=1}^{T-2\Delta t} \left( \text{Cov}(\hat{\epsilon}_{1,t+\Delta t}^2, \hat{\epsilon}_{1,t+\Delta t}^2) - 4 \times \right. \\ &\quad \left. \Delta \hat{I}_1(\mathbf{q}, t, \Delta t) \Delta \hat{I}_1(\mathbf{q}, t + \Delta t, \Delta t) \text{Cov}(\hat{\epsilon}_{1,t+\Delta t}, \hat{\epsilon}_{1,t+\Delta t}) \right) \\ &= 2 \sum_{t=1}^{T-2\Delta t} \left( \frac{\sigma_0^4}{2} - 4\sigma_0^2 \Delta \hat{I}_1(\mathbf{q}, t, \Delta t) \Delta \hat{I}_1(\mathbf{q}, t + \Delta t, \Delta t) \right), \end{aligned}$$

with

$$\begin{aligned} \hat{\epsilon}_{1,t} &= \frac{1}{N} \sum_{x_1=1}^{N-1} \sum_{x_2=1}^{N-1} \epsilon(\mathbf{x}, t) \cos\left(\frac{2\pi \mathbf{x}^T \mathbf{q}}{N}\right) \\ \hat{\epsilon}_{2,t} &= \frac{1}{N} \sum_{x_1=1}^{N-1} \sum_{x_2=1}^{N-1} \epsilon(\mathbf{x}, t) \sin\left(\frac{2\pi \mathbf{x}^T \mathbf{q}}{N}\right). \end{aligned}$$

Similarly, for  $\Delta t = 1, 2, \dots, \lfloor (t_{max} - 1)/2 \rfloor$  and  $t_{max} = T$

$$\begin{aligned} & \sum_{t_1 \neq t_2} \text{Cov}(\Delta \hat{I}_{o,2}^2(\mathbf{q}, t_1, \Delta t), \Delta \hat{I}_{o,2}^2(\mathbf{q}, t_2, \Delta t)) \\ &= 2 \sum_{t=1}^{T-2\Delta t} \left( \frac{\sigma_0^4}{2} - 4\sigma_0^2 \Delta \hat{I}_2(\mathbf{q}, t, \Delta t) \Delta \hat{I}_2(\mathbf{q}, t + \Delta t, \Delta t) \right) \end{aligned}$$

For general  $\Delta t > \lfloor (T - 1)/2 \rfloor$ :

$$\begin{aligned} & \sum_{t_1 \neq t_2} \text{Cov}(\Delta \hat{I}_{o,1}^2(\mathbf{q}, t_1, \Delta t), \Delta \hat{I}_{o,1}^2(\mathbf{q}, t_2, \Delta t)) \\ &= \sum_{t_1 \neq t_2} \text{Cov}(\Delta \hat{I}_{o,2}^2(\mathbf{q}, t_1, \Delta t), \Delta \hat{I}_{o,2}^2(\mathbf{q}, t_2, \Delta t)) \\ &= 0 \end{aligned}$$

Combining the variance and covariance expressions developed above, the variance of the average of intensity is

$$\begin{aligned} & \mathbb{V} \left[ \frac{1}{n_{\Delta t}} \sum_{t \in S_{\Delta t}} |\Delta \hat{I}_o(\mathbf{q}, t, \Delta t)|^2 \right] \\ &= \frac{2\sigma_0^2}{n_{\Delta t}} \left( 2\sigma_0^2 + \frac{2 \sum_{t=1}^{n_{\Delta t}} |\Delta \hat{I}(\mathbf{q}, t, \Delta t)|^2}{n_{\Delta t}} \right. \\ & \quad \left. + \max(0, T - 2\Delta t) \left( \frac{\sigma_0^2}{n_{\Delta t}} - \frac{2S_{q_1, q_2, \Delta t}}{n_{\Delta t}(T - 2\Delta t)} \right) \right) \end{aligned}$$

with

$$\begin{aligned} S_{q_1, q_2, \Delta t} &= \sum_{t=1}^{T-2\Delta t} \left( \Delta \hat{I}_1(\mathbf{q}, t, \Delta t) \Delta \hat{I}_1(\mathbf{q}, t + \Delta t, \Delta t) \right. \\ & \quad \left. + \Delta \hat{I}_2(\mathbf{q}, t, \Delta t) \Delta \hat{I}_2(\mathbf{q}, t + \Delta t, \Delta t) \right) \quad (33) \end{aligned}$$

Finally, we have

$$\begin{aligned} & \mathbb{V}[D_o(q, \Delta t)] \\ &= \mathbb{V} \left[ \frac{1}{n_q} \sum_{(q_1, q_2) \in S_q} \frac{1}{n_{\Delta t}} \sum_{t \in S_{\Delta t}} |\Delta \hat{I}_o(\mathbf{q}, t, \Delta t)|^2 \right] \\ &= \frac{1}{n_q^2} \sum_{(q_1, q_2) \in S_q} \frac{2\sigma_0^2}{n_{\Delta t}} \left( 2\sigma_0^2 + \frac{2 \sum_{t=1}^{n_{\Delta t}} |\Delta \hat{I}(\mathbf{q}, t, \Delta t)|^2}{n_{\Delta t}} \right. \\ & \quad \left. + \max(0, T - 2\Delta t) \left( \frac{\sigma_0^2}{n_{\Delta t}} - \frac{2S_{q_1, q_2, \Delta t}}{n_{\Delta t}(T - 2\Delta t)} \right) \right) \\ &= \frac{2\sigma_0^2}{n_q n_{\Delta t}} \left( 2\sigma_0^2 + 2D(q, \Delta t) \right. \\ & \quad \left. + \max(0, T - 2\Delta t) \left( \frac{\sigma_0^2}{n_{\Delta t}} - \frac{2S_{q, \Delta t}}{(T - 2\Delta t)n_{\Delta t}n_q} \right) \right) \end{aligned}$$

with

$$S_{q, \Delta t} = \sum_{(q_1, q_2): q_1^2 + q_2^2 = q^2} S_{q_1, q_2, \Delta t} \quad (34)$$

□

## APPENDIX B DERIVATION OF MEAN SQUARED DISPLACEMENT

Here we derive the MSD for each of the different scenarios explored in simulation. First, the simulated particles in Sections IIIB and IIIC all undergo Brownian motion. Without loss of generality, we may assume the variance of  $\Delta x_{i,j}(t)$  is  $\sigma_s^2$ . For any  $\mathbf{x}(t), \mathbf{x}(t + \Delta t) \in \mathbb{R}^2$ , the MSD can be simply computed by

$$\begin{aligned} & \mathbb{E}[(x_{ij}(t + \Delta t) - x_{ij}(t))^2] \\ &= \mathbb{V}[x_{ij}(t + \Delta t) - x_{ij}(t)] + \{\mathbb{E}[x_{ij}(t + \Delta t) - x(t)]\}^2 \\ &= \mathbb{V} \left[ \sum_{k=0}^{\Delta t-1} \Delta x_{ij}(t + k) \right] + 0 \\ &= \sigma_s^2 \Delta t \end{aligned}$$

for any  $j = 1, \dots, p$  and  $i = 1, 2$ . Since particles move isotropically in a two dimensional space, the MSD is  $2\sigma_s^2 \Delta t$ .

In simulated scenarios presented in Section IIID, similarly we can split the MSD into two terms. Noting  $\mathbb{E}[x_{ij}(t + \Delta t) - x_{ij}(t)] = \mu_D \Delta t$  and the process is isotropic, the MSD is  $2\sigma_s^2 \Delta t + 2\mu_D^2 \Delta t^2$ ,

In simulated scenarios presented in Section IIIE, note that when  $t = t_1$ ,  $x_{ij}(t_1) \sim N(x_{ij}(t_0), \sigma_D^2)$ . For any  $t > t_1$ , it is not hard to show

$$\begin{aligned} \mathbb{E}[x_{1j}(t)] &= (t - 1)\mu_D \cos(\theta_j) + x_{1j}(t_0) \\ \mathbb{E}[x_{2j}(t)] &= (t - 1)\mu_D \sin(\theta_j) + x_{2j}(t_0) \end{aligned}$$

and consequently

$$\mathbb{E} \left[ \sum_{i=1}^2 (x_{ij}(t + \Delta t) - x_{ij}(t))^2 \right] = \mu_D^2 \Delta t^2 \quad (35)$$

And it is easy to verify  $\mathbb{V}[x_{ij}(t)] = \sigma_s^2$ . Thus we have

$$\begin{aligned} & \mathbb{V}[x_{ij}(t + \Delta t) - x_{ij}(t)] \\ &= \mathbb{V}[x_{ij}(t + \Delta t)] + \mathbb{V}[x_{ij}(t)] - 2\text{Cov}(x_{ij}(t + \Delta t), x_{ij}(t)) \\ &= 2\sigma_s^2 - 2\text{Cov}(\rho^{\Delta t} x_{ij}(t), x_{ij}(t)) \\ &= 2\sigma_s^2 - 2\sigma_s^2 \rho^{\Delta t} \quad (36) \end{aligned}$$

Since the process is on a two dimensional space, combining (35) and (36), the MSD is  $4\sigma_s^2 - 4\sigma_s^2 \rho^{\Delta t} + \mu_D^2 \Delta t^2$ .

## APPENDIX C

The notations used in this paper are listed in Table III.

TABLE III. Table of notations

<i>Brackets, overheads &amp; superscripts</i>	
$\sim$	logarithmically transformed variables
$\hat{\phantom{x}}$	Fourier transformed functions
$\langle \dots \rangle_i$	ensemble average with respect to variable $i$
$ \dots $	modulus of complex numbers
$\dots_o$	observed quantities
$\dots_*$	unknown variables
$\dots_e$	estimated quantities
$\Delta$	difference of functions or variables
$\dots^T$	transpose
<i>Variables</i>	
$\mathbf{x}$	coordinates in real-space
$\mathbf{q}$	coordinates in Fourier transformed (reciprocal) space
$q$	radius of coordinates in Fourier transformed space
$t$	real time in experiments
$t_{min}$	starting time in experiments
$t_{max}$	ending time in experiments
$T$	the total number of time points in experiments
$\Delta t$	lag time
$\epsilon$	noise in the image intensity
$\sigma_o^2$	variance of the noise in the image intensity
$n_p$	number of particles
$n_{\Delta t}$	number of lag time points when lag time is $\Delta t$
$n_q$	number of coordinates with radius $q$
$\tau$	range parameter in a stretched exponential model
$\gamma$	roughness parameter in a stretched exponential model
$\mathcal{S}$	sets of variables
$\Delta\mathcal{T}$	sets of available $\Delta t$ 's
$\mathcal{Q}$	sets of available $q$ 's
<i>Particle Dynamics Simulations</i>	
$\sigma_s$	diffusive step size
$\mu_D$	drift velocity
$D_m$	diffusion coefficient
$I_p(\mathbf{x}, t)$	particle intensity function
$I_c$	particle center pixel intensity used in $I_p(\mathbf{x}, t)$
$I_b(\mathbf{x}, t)$	background intensity function
<i>Gaussian Process Regression</i>	
$\mu$	mean parameter
$\sigma^2$	variance parameter
$\beta$	inverse range parameters
$\eta$	nugget parameter
$\epsilon_\theta$	noise in regression
$S^2$	sample variance
$\mathbf{D}_o$	vector of observed image structure function
<i>Constants</i>	
$k_B$	Boltzmann constant
$T_a$	absolute temperature
<i>Functions &amp; Operators</i>	
$I(\mathbf{x}, t)$	image intensity function
$D(\mathbf{q}, \Delta t)$	image structure function
$D_o(\mathbf{q}, \Delta t)$	observed image structure function (which contains noise)
$D_e(\mathbf{q}, \Delta t)$	estimated image structure function fit by parameterized model
$f(\mathbf{q}, \Delta t)$	intermediate scattering function
$\langle \Delta r^2(\Delta t) \rangle$	mean squared displacement
$\mathcal{F}(\dots)$	operator of the 2D discrete Fourier transform
$\mathcal{L}(\dots)$	likelihood function
$\mathcal{N}$	normal distribution
$\mathbb{V}(\dots)$	variance of variables
$\mathbb{E}(\dots)$	expected value of variables